

$\Lambda_b \rightarrow \Lambda \ell^+ \ell^-$ form factors and differential branching fraction from lattice QCDWilliam Detmold,¹ C.-J. David Lin,^{2,3} Stefan Meinel,^{1,*} and Matthew Wingate⁴¹*Center for Theoretical Physics, Massachusetts Institute of Technology, Cambridge, MA 02139, USA*²*Institute of Physics, National Chiao-Tung University, Hsinchu 300, Taiwan*³*Physics Division, National Centre for Theoretical Sciences, Hsinchu 300, Taiwan*⁴*DAMTP, University of Cambridge, Wilberforce Road, Cambridge CB3 0WA, UK*

(Dated: December 19, 2012)

We present the first lattice QCD determination of the $\Lambda_b \rightarrow \Lambda$ transition form factors that govern the rare baryonic decays $\Lambda_b \rightarrow \Lambda \ell^+ \ell^-$ at leading order in heavy-quark effective theory. Our calculations are performed with 2+1 flavors of domain-wall fermions, at two lattice spacings and with pion masses down to 227 MeV. Three-point functions with a wide range of source-sink separations are used to extract the ground-state contributions. The form factors are extrapolated to the physical values of the light-quark masses and to the continuum limit. We use our results to calculate the differential branching fractions for $\Lambda_b \rightarrow \Lambda \ell^+ \ell^-$ with $\ell = e, \mu, \tau$ within the standard model. We find agreement with a recent CDF measurement of the $\Lambda_b \rightarrow \Lambda \mu^+ \mu^-$ differential branching fraction.

PACS numbers: 12.38.Gc, 12.39.Fe, 12.39.Hg, 14.20.Mr

I. INTRODUCTION

The flavor-changing neutral-current transitions $b \rightarrow s \gamma$ and $b \rightarrow s \ell^+ \ell^-$ can provide strong constraints on models of new physics. The effective weak Hamiltonian describing decays of this type has the form [1–8]

$$\mathcal{H}_{\text{eff}} = -\frac{4G_F}{\sqrt{2}} V_{tb} V_{ts}^* \sum_{i=1, \dots, 10, S, P} (C_i O_i + C'_i O'_i), \quad (1)$$

where the operators that directly give “short-distance” contributions to these decay amplitudes are

$$\begin{aligned} O_7 &= \frac{e}{16\pi^2} m_b \bar{s} \sigma^{\mu\nu} P_R b F_{\mu\nu}^{(\text{e.m.})}, & O'_7 &= \frac{e}{16\pi^2} m_b \bar{s} \sigma^{\mu\nu} P_L b F_{\mu\nu}^{(\text{e.m.})}, \\ O_9 &= \frac{e^2}{16\pi^2} \bar{s} \gamma^\mu P_L b \bar{l} \gamma_\mu l, & O'_9 &= \frac{e^2}{16\pi^2} \bar{s} \gamma^\mu P_R b \bar{l} \gamma_\mu l, \\ O_{10} &= \frac{e^2}{16\pi^2} \bar{s} \gamma^\mu P_L b \bar{l} \gamma_\mu \gamma_5 l, & O'_{10} &= \frac{e^2}{16\pi^2} \bar{s} \gamma^\mu P_R b \bar{l} \gamma_\mu \gamma_5 l, \\ O_S &= \frac{e^2}{16\pi^2} m_b \bar{s} P_R b \bar{l} l, & O'_S &= \frac{e^2}{16\pi^2} m_b \bar{s} P_L b \bar{l} l, \\ O_P &= \frac{e^2}{16\pi^2} m_b \bar{s} P_R b \bar{l} \gamma_5 l, & O'_P &= \frac{e^2}{16\pi^2} m_b \bar{s} P_L b \bar{l} \gamma_5 l, \end{aligned} \quad (2)$$

and the $C_i^{(\prime)}$ are Wilson coefficients. In the standard model, the Wilson coefficients of the scalar and pseudoscalar operators $O_{S,P}$, as well as those of the opposite-chirality operators O'_i , are highly suppressed [9]. Experimental measurements of $b \rightarrow s$ decay rates, angular distributions, and related observables provide constraints on various functions of the Wilson coefficients C_i and C'_i [9]. In this way, these measurements restrict models of new physics and their allowed parameters. Most of the existing studies have focused on mesonic decays such as $B \rightarrow K^* \gamma$ and $B \rightarrow K^{(*)} \ell^+ \ell^-$, for which experiments have reached a high level of precision. To get the most complete set of constraints on new physics, it is important to consider many different observables. To this end it is useful to analyze also *baryonic* $b \rightarrow s$ decays such as $\Lambda_b \rightarrow \Lambda \gamma$ and $\Lambda_b \rightarrow \Lambda \ell^+ \ell^-$. The decay $\Lambda_b \rightarrow \Lambda \mu^+ \mu^-$ has recently been observed using the Tevatron [10], and is being measured at LHCb.

One important aspect that distinguishes Λ_b decays from B meson decays is the spin of the Λ_b baryon, which in principle provides an additional handle on the fundamental interactions. When produced through Z bosons at $e^+ e^-$ colliders, b quarks have a strong longitudinal polarization, and the Λ_b baryons keep most of that polarization [11–16].

* smeinel@mit.edu

At the Tevatron and the LHC, the Λ_b baryons produced in proton-(anti)proton collisions are expected to have some degree of transverse polarization [17–19], which can be measured accurately using the method proposed in Ref. [20]. As first mentioned in Ref. [21] and later studied in detail in Ref. [22], the Λ_b polarization can be exploited to test the “helicity structure” of \mathcal{H}_{eff} , that is, to disentangle the contributions from the Wilson coefficients C_i and C'_i . In practice, this entails measuring an asymmetry in the angular distribution between the Λ_b spin and the momentum of a particle in the final state [22]. Even for unpolarized Λ_b baryons, the spin of the final-state Λ baryon can also be exploited to test the helicity structure of \mathcal{H}_{eff} , as discussed for $\Lambda_b \rightarrow \Lambda \gamma$ in Refs. [22–27] and for $\Lambda_b \rightarrow \Lambda \ell^+ \ell^-$ in Refs. [25, 26, 28–30]. To this end, an angular analysis needs to be performed for the secondary weak decay $\Lambda \rightarrow p \pi^-$. Lepton asymmetries for $\Lambda_b \rightarrow \Lambda \ell^+ \ell^-$ have also been considered [26, 30–32].

In order to use these Λ_b decays to search for new physics, the matrix elements $\langle \Lambda \gamma | \mathcal{H}_{\text{eff}} | \Lambda_b \rangle$ or $\langle \Lambda \ell^+ \ell^- | \mathcal{H}_{\text{eff}} | \Lambda_b \rangle$ must be determined. For the operators in Eq. (2), this then requires the computation of the hadronic matrix elements $\langle \Lambda | \bar{s} \Gamma b | \Lambda_b \rangle$, which are expressed in terms of ten QCD form factors. When using heavy-quark effective theory (HQET) for the b quark, the number of independent $\Lambda_b \rightarrow \Lambda$ form factors reduces to 2 [33–35]. Furthermore, in the limit of large recoil, soft-collinear effective theory (SCET) predicts that only one form factor remains [27, 36, 37]. The $\Lambda_b \rightarrow \Lambda$ form factors have been estimated using various models or approximations, including quark models [38–41], perturbative QCD [42], and sum rules [25, 26, 36, 43], but have not been determined from QCD previously. In the charm sector, some information on the $\Lambda_c \rightarrow \Lambda$ form factors is available from the experimental measurement of the semileptonic $\Lambda_c \rightarrow \Lambda e^+ \nu_e$ decay [44, 45], and this information has been used to constrain the $\Lambda_b \rightarrow \Lambda$ form factors in Refs. [23, 38]. In summary, several estimates of $\Lambda_b \rightarrow \Lambda$ form factors exist in the literature, but a considerable uncertainty remains, especially in the low-recoil region where SCET and light-cone sum rules are not applicable. Clearly, first-principles, nonperturbative QCD calculations of the form factors are needed, and the method for performing such calculations is lattice QCD.

In this paper, we report on the first lattice QCD calculation of $\Lambda_b \rightarrow \Lambda$ form factors (we presented preliminary results of this work in Ref. [46]). We use HQET for the b quark, and compute the two form factors that appear. Their definitions are given in Sec. II. Treating the b quarks with HQET on the lattice [47] also leads to several other technical simplifications that make the calculation feasible, as will become clear in Sec. III A. For the up, down, and strange quarks, we use a domain-wall fermion action [48–50], which is computationally expensive but provides chiral symmetry even at non-zero lattice spacing. Our calculations make use of gauge field ensembles generated by the RBC/UKQCD collaborations [51]. These ensembles include 2+1 flavors of dynamical sea quarks, and the lattice parameters used in our study are given in Sec. III B. We use two different lattice spacings and several different values of the light quark masses, which allows us to perform simultaneous extrapolations of the form factors to the continuum limit and to the physical values of the quark masses. The data analysis involves several stages, which are explained in Secs. III C, III D, III E, and III F, and estimates of the systematic uncertainties in the form factors are given in Sec. III G. As a first application of our form factor results, in Sec. IV we then calculate the differential branching fractions for the decays $\Lambda_b \rightarrow \Lambda \ell^+ \ell^-$ with $\ell = e, \mu, \tau$ in the standard model. The differential branching fraction for $\Lambda_b \rightarrow \Lambda \mu^+ \mu^-$ can be compared to the existing Tevatron data and is of immediate interest for LHCb. Further phenomenological applications of the form factors that we have determined are left for future work.

II. DEFINITION OF FORM FACTORS

In QCD, using Lorentz symmetry and the discrete C, P, T symmetries, one can show that the matrix elements $\langle \Lambda(p', s') | \bar{s} \Gamma b | \Lambda_b(p, s) \rangle$ with $\Gamma = \gamma_\mu, \gamma_\mu \gamma_5, q^\nu \sigma_{\mu\nu}, q^\nu \sigma_{\mu\nu} \gamma_5$ (where $q = p - p'$) are parametrized by ten independent form factors (see for example Ref. [36]). Heavy-quark symmetry, which becomes exact in the limit $m_b \rightarrow \infty$, reduces the number of independent form factors to 2 [33–35]. In the following, when working with HQET, we denote the heavy quark by Q . The $\Lambda_Q \rightarrow \Lambda$ matrix element with an arbitrary Dirac matrix Γ is then given by [33–35]

$$\langle \Lambda(p', s') | \bar{s} \Gamma Q | \Lambda_Q(v, 0, s) \rangle = \bar{u}(p', s') [F_1(p' \cdot v) + \not{v} F_2(p' \cdot v)] \Gamma \mathcal{U}(v, s), \quad (3)$$

where v is the four-velocity of the Λ_Q , and the two form factors F_1 and F_2 can be expressed as functions solely of $p' \cdot v$, the energy of the Λ baryon in the Λ_Q rest frame. Here we use the following normalization of states and spinors:

$$\langle \Lambda(p, s) | \Lambda(p', s') \rangle = 2E_\Lambda (2\pi)^3 \delta_{ss'} \delta^3(\mathbf{p} - \mathbf{p}'), \quad (4)$$

$$\langle \Lambda_Q(v, k, s) | \Lambda_Q(v, k', s') \rangle = 2v^0 (2\pi)^3 \delta_{ss'} \delta^3(\mathbf{k} - \mathbf{k}'), \quad (5)$$

$$\sum_{s'=1}^2 u(p', s') \bar{u}(p', s') = m_\Lambda + \not{p}', \quad (6)$$

$$\sum_{s=1}^2 \mathcal{U}(v, s) \bar{\mathcal{U}}(v, s) = 1 + \not{v}. \quad (7)$$

For most of the analysis in this paper, it is convenient to work with the linear combinations

$$\begin{aligned} F_+ &= F_1 + F_2, \\ F_- &= F_1 - F_2, \end{aligned} \quad (8)$$

instead of F_1 and F_2 . Note that in the limit $m_b \rightarrow \infty$, five of the ten helicity-based $\Lambda_b \rightarrow \Lambda$ form factors introduced in Ref. [36] become equal to F_+ , while the other five become equal to F_- [see Eq. (2.10) of Ref. [36], where F_1 is denoted by A , and F_2 is denoted by B].

III. LATTICE CALCULATION

A. Two-point and three-point functions

For the lattice calculation, we work in the Λ_Q rest frame, so that $v = (1, 0, 0, 0)$. The heavy quark, Q , is implemented with the Eichten-Hill lattice HQET action [47], where we use one level of HYP smearing [52] for the temporal gauge links in order to improve the signal-to-noise ratio of the correlation functions [53]. For the up, down, and strange quarks, we use a domain-wall action [48–50], and the gluons are implemented using the Iwasaki action [54, 55]. Our calculations are based on gauge field configurations generated by the RBC/UKQCD collaboration [51] using these actions. Further details of the lattices will be given in Sec. III B.

In order to extract the matrix element (3), we need to compute suitable three-point- and two-point-functions as discussed in the following. We use the following baryon interpolating fields,

$$\Lambda_{Q\alpha} = \epsilon^{abc} (C\gamma_5)_{\beta\gamma} \tilde{d}_\beta^a \tilde{u}_\gamma^b Q_\alpha^c, \quad (9)$$

$$\Lambda_\alpha = \epsilon^{abc} (C\gamma_5)_{\beta\gamma} \tilde{u}_\beta^a \tilde{d}_\gamma^b \tilde{s}_\alpha^c, \quad (10)$$

where a, b, c are color indices, α, β, γ are spinor indices, and C is the charge conjugation matrix. The tilde on the up, down, and strange quark fields u, d, s denotes gauge-covariant three-dimensional Gaussian smearing, intended to reduce excited-state contamination in the correlation functions.

In the three-point functions, we use the following $\mathcal{O}(a)$ -improved discretization of the continuum HQET current [56],

$$J_\Gamma^{(\text{HQET})}(m_b) = U(m_b, a^{-1}) \mathcal{Z} \left[J_\Gamma^{(\text{LHQET})} + c_\Gamma^{(m_s a)} \frac{m_s a}{1 - (w_0^{\text{MF}})^2} J_\Gamma^{(\text{LHQET})} + c_\Gamma^{(p_s a)} a J_{\Gamma D}^{(\text{LHQET})} \right], \quad (11)$$

where $J_\Gamma^{(\text{LHQET})}$ and $J_{\Gamma D}^{(\text{LHQET})}$ are given by

$$J_\Gamma^{(\text{LHQET})} = \bar{Q} \Gamma s, \quad (12)$$

$$J_{\Gamma D}^{(\text{LHQET})} = \bar{Q} \Gamma \gamma \cdot \nabla s. \quad (13)$$

The current $J_\Gamma^{(\text{HQET})}$ is renormalized in the $\overline{\text{MS}}$ scheme at $\mu = m_b$. Note that here we match from lattice HQET to continuum HQET, but not yet to QCD. This is important because the form factors F_1 and F_2 are defined in continuum HQET, not full QCD. The matching to QCD will lead to radiative corrections to the simple relationship (3) which depend on Γ . We will return to this issue in Sec. IV when computing the differential branching fraction for $\Lambda_b \rightarrow \Lambda \ell^+ \ell^-$.

In Eq. (11), symmetries of the lattice actions and the equations of motion have been used to reduce the number of operators that appear [56]. The term with coefficient $c_\Gamma^{(m_s a)}$ provides $\mathcal{O}(m_s a)$ improvement, while the term with coefficient $c_\Gamma^{(p_s a)}$ provides $\mathcal{O}(p_s a)$ improvement (here p_s denotes the momentum of the strange quark). The quantity w_0^{MF} is related to tadpole improvement, and is defined as $w_0^{\text{MF}} = 1 - am_5 + 4(1 - u_0)$ [56], where am_5 is the domain-wall height and u_0 is the 4th root of the average plaquette. The matching coefficients \mathcal{Z} , $c_\Gamma^{(m_s a)}$, and $c_\Gamma^{(p_s a)}$ have been computed to one-loop order in lattice perturbation theory for the actions used here in Ref. [56] and are evaluated

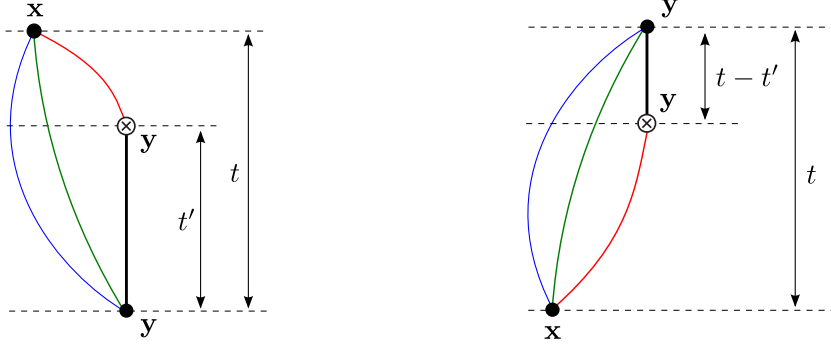


FIG. 1. Propagator contractions for the forward three-point functions (left) and backward three-point functions (right). The thick vertical line at the spatial point \mathbf{y} indicates the static heavy-quark propagator. The source for all light and strange-quark propagators is located at the fixed point (x_0, \mathbf{x}) . We sum over all points \mathbf{y} , with the appropriate momentum phases as in Eqs. (18) and (19).

at the scale $\mu = a^{-1}$ (the inverse lattice spacing). The coefficient \mathcal{Z} is independent of Γ , but $c_\Gamma^{(m_s a)}$ and $c_\Gamma^{(p_s a)}$ change sign depending on whether Γ commutes or anticommutes with γ^0 . We are interested in the matrix element (3) renormalized at $\mu = m_b$, and following Ref. [56] we therefore perform a renormalization-group (RG) evolution from $\mu = a^{-1}$ to $\mu = m_b$, using the two-loop anomalous dimension of the heavy-light current in HQET, which was derived in Refs. [57, 58]. This leads to the multiplicative factor $U(m_b, a^{-1})$ in Eq. (11). The RG running is performed with $N_f = 3$ flavors from $\mu = a^{-1}$ down to $\mu = m_c$, and then with $N_f = 4$ flavors from $\mu = m_c$ up to $\mu = m_b$. This two-step running is used because the nonperturbative lattice calculations are done with $N_f = 2 + 1$ dynamical flavors, and with $a^{-1} > m_c$. However, note that doing a simple $N_f = 4$ running from $\mu = a^{-1}$ to $\mu = m_b$ gives a result that differs only by 0.5%. Numerical values for $U(m_b, a^{-1})$, \mathcal{Z} , $c_\Gamma^{(m_s a)}$, $c_\Gamma^{(p_s a)}$, and u_0 will be given in Table II in the next section.

Having defined the interpolating fields and the current, we will now discuss the correlation functions. We compute “forward” and “backward” two-point functions for the Λ and Λ_Q as follows:

$$C_{\delta\alpha}^{(2,\Lambda)}(\mathbf{p}', t) = \sum_{\mathbf{y}} e^{-i\mathbf{p}' \cdot (\mathbf{y} - \mathbf{x})} \langle \Lambda_\delta(x_0 + t, \mathbf{y}) \bar{\Lambda}_\alpha(x_0, \mathbf{x}) \rangle, \quad (14)$$

$$C_{\delta\alpha}^{(2,\Lambda, \text{bw})}(\mathbf{p}', t) = \sum_{\mathbf{y}} e^{-i\mathbf{p}' \cdot (\mathbf{x} - \mathbf{y})} \langle \Lambda_\delta(x_0, \mathbf{x}) \bar{\Lambda}_\alpha(x_0 - t, \mathbf{y}) \rangle, \quad (15)$$

$$C_{\delta\alpha}^{(2,\Lambda_Q)}(t) = \langle \Lambda_{Q\delta}(x_0 + t, \mathbf{x}) \bar{\Lambda}_{Q\alpha}(x_0, \mathbf{x}) \rangle, \quad (16)$$

$$C_{\delta\alpha}^{(2,\Lambda_Q, \text{bw})}(t) = \langle \Lambda_{Q\delta}(x_0, \mathbf{x}) \bar{\Lambda}_{Q\alpha}(x_0 - t, \mathbf{x}) \rangle, \quad (17)$$

where the superscript “bw” denotes the backward correlator. In Eqs. (16) and (17), the Λ_Q interpolating fields at source and sink are required to be at the same spatial point \mathbf{x} because of the static heavy-quark propagator. Finally, the forward and backward three-point functions for a given gamma matrix Γ in the current are defined as

$$C_{\delta\alpha}^{(3)}(\Gamma, \mathbf{p}', t, t') = \sum_{\mathbf{y}} e^{-i\mathbf{p}' \cdot (\mathbf{x} - \mathbf{y})} \langle \Lambda_\delta(x_0, \mathbf{x}) J_\Gamma^{(\text{HQET})\dagger}(x_0 - t + t', \mathbf{y}) \bar{\Lambda}_{Q\alpha}(x_0 - t, \mathbf{y}) \rangle, \quad (18)$$

$$C_{\alpha\delta}^{(3, \text{bw})}(\Gamma, \mathbf{p}', t, t') = \sum_{\mathbf{y}} e^{-i\mathbf{p}' \cdot (\mathbf{y} - \mathbf{x})} \langle \Lambda_{Q\alpha}(x_0 + t, \mathbf{y}) J_\Gamma^{(\text{HQET})}(x_0 + t', \mathbf{y}) \bar{\Lambda}_\delta(x_0, \mathbf{x}) \rangle. \quad (19)$$

All of the above correlation functions (14)-(19) can be computed using light and strange quark propagators with a Gaussian-smeared source located at (x_0, \mathbf{x}) . For the three-point functions, the quark propagator contractions are illustrated schematically in Fig. 1. Because no additional domain-wall propagators are required, we can efficiently compute the three-point functions for arbitrary values of t and t' , only limited by statistical precision.

In order to discuss the spectral decomposition of the correlation functions, we introduce the following definitions for the overlap factors:

$$\langle 0 | \Lambda_{Q\alpha}(0) | \Lambda_Q(s) \rangle = Z_{\Lambda_Q} \mathcal{U}_\alpha(s), \quad (20)$$

$$\langle 0 | \Lambda_\alpha(0) | \Lambda(p', s) \rangle = [(Z_\Lambda^{(1)} + Z_\Lambda^{(2)} \gamma^0) u(p', s)]_\alpha, \quad (21)$$

where $Z_\Lambda^{(1)}$ and $Z_\Lambda^{(2)}$ depend on \mathbf{p}' . Here we need two different overlap factors $Z_\Lambda^{(1)}$ and $Z_\Lambda^{(2)}$ for the Λ , because the spatial-only smearing of the quarks in the interpolating field (10) breaks hypercubic symmetry [59]. The spectral decompositions of the two-point and three-point functions then read

$$C_{\delta\alpha}^{(2,\Lambda)}(\mathbf{p}', t) = C_{\delta\alpha}^{(2,\Lambda,\text{bw})}(\mathbf{p}', t) = \frac{1}{2E_\Lambda} e^{-E_\Lambda t} \left[(Z_\Lambda^{(1)} + Z_\Lambda^{(2)}\gamma^0)(m_\Lambda + \not{p}')(Z_\Lambda^{(1)} + Z_\Lambda^{(2)}\gamma^0) \right]_{\delta\alpha} + \dots, \quad (22)$$

$$C_{\delta\alpha}^{(2,\Lambda_Q)}(t) = C_{\delta\alpha}^{(2,\Lambda_Q,\text{bw})}(t) = \frac{1}{2} e^{-E_{\Lambda_Q} t} Z_{\Lambda_Q}^2 [1 + \gamma^0]_{\delta\alpha} + \dots, \quad (23)$$

$$C_{\delta\alpha}^{(3)}(\Gamma, \mathbf{p}', t, t') = Z_{\Lambda_Q} \frac{1}{2E_\Lambda} \frac{1}{2} e^{-E_\Lambda(t-t')} e^{-E_{\Lambda_Q} t'} \left[(Z_\Lambda^{(1)} + Z_\Lambda^{(2)}\gamma^0)(m_\Lambda + \not{p}')(F_1 + \gamma^0 F_2) \Gamma (1 + \gamma^0) \right]_{\delta\alpha} + \dots, \quad (24)$$

$$C_{\alpha\delta}^{(3,\text{bw})}(\Gamma, \mathbf{p}', t, t-t') = Z_{\Lambda_Q} \frac{1}{2E_\Lambda} \frac{1}{2} e^{-E_{\Lambda_Q}(t-t')} e^{-E_\Lambda t'} \left[(1 + \gamma^0) \bar{\Gamma} (F_1 + \gamma^0 F_2)(m_\Lambda + \not{p}')(Z_\Lambda^{(1)} + Z_\Lambda^{(2)}\gamma^0) \right]_{\alpha\delta} + \dots, \quad (25)$$

where we have only shown the ground-state contributions, and the ellipsis denote excited-state contributions that decay exponentially faster with the Euclidean time separations. For the three-point functions, we have used Eq. (3) to express the current matrix element in terms of the form factors F_1 and F_2 .

Using the three-point and two-point functions, we then define the following ratio,

$$\mathcal{R}(\Gamma, \mathbf{p}', t, t') = \frac{4 \text{Tr} [C^{(3)}(\Gamma, \mathbf{p}', t, t') C^{(3,\text{bw})}(\Gamma, \mathbf{p}', t, t-t')]}{\text{Tr}[C^{(2,\Lambda,\text{av})}(\mathbf{p}', t)] \text{Tr}[C^{(2,\Lambda_Q,\text{av})}(t)]}, \quad (26)$$

where the traces are over spinor indices, and the two-point functions in the denominator are the averages of the forward- and backward two-point functions (to increase statistics). For the ground-state contributions, the product of forward and backward three-point functions in the numerator of Eq. (26) eliminates the t' -dependence, and dividing by the two-point functions evaluated at the same t also cancels the t -dependence and Z -factors. For gamma matrices Γ that commute (anticommute) with γ^0 , the ground-state contribution in the ratio $\mathcal{R}(\Gamma, \mathbf{p}', t, t')$ will be proportional to $[F_+]^2$ ($[F_-]^2$). Thus, we form the combinations

$$\mathcal{R}_+(\mathbf{p}', t, t') = \frac{1}{4} [\mathcal{R}(1, \mathbf{p}', t, t') + \mathcal{R}(\gamma^2 \gamma^3, \mathbf{p}', t, t') + \mathcal{R}(\gamma^3 \gamma^1, \mathbf{p}', t, t') + \mathcal{R}(\gamma^1 \gamma^2, \mathbf{p}', t, t')], \quad (27)$$

$$\mathcal{R}_-(\mathbf{p}', t, t') = \frac{1}{4} [\mathcal{R}(\gamma^1, \mathbf{p}', t, t') + \mathcal{R}(\gamma^2, \mathbf{p}', t, t') + \mathcal{R}(\gamma^3, \mathbf{p}', t, t') + \mathcal{R}(\gamma_5, \mathbf{p}', t, t')], \quad (28)$$

which are equal to

$$\mathcal{R}_+(\mathbf{p}', t, t') = \frac{E_\Lambda + m_\Lambda}{E_\Lambda} [F_+]^2 + \dots, \quad (29)$$

$$\mathcal{R}_-(\mathbf{p}', t, t') = \frac{E_\Lambda - m_\Lambda}{E_\Lambda} [F_-]^2 + \dots, \quad (30)$$

where, as before, the ellipsis denote excited-state contributions. Note that multiplying the gamma matrices in Eqs. (27) and (28) with γ^0 would not give any new information, because $\gamma^0 Q = Q$. Next, we average (27) and (28) over momenta \mathbf{p}' with fixed magnitude $|\mathbf{p}'|$, and replace the label \mathbf{p}' by $|\mathbf{p}'|^2$ to denote the direction-averaged quantities,

$$\mathcal{R}_\pm(|\mathbf{p}'|^2, t, t'). \quad (31)$$

Finally, we evaluate $\mathcal{R}_\pm(|\mathbf{p}'|^2, t, t')$ at $t' = t/2$ (or average it over $(t-a)/2$ and $(t+a)/2$ for odd values of t/a) where the excited-state contamination is smallest, rescale using $E_\Lambda(|\mathbf{p}'|^2)$ and m_Λ obtained from fits to the two-point functions, and take the square root to obtain

$$R_+(|\mathbf{p}'|^2, t) = \sqrt{\frac{E_\Lambda}{E_\Lambda + m_\Lambda} \mathcal{R}_+(|\mathbf{p}'|^2, t, t/2)}, \quad (32)$$

$$R_- (|\mathbf{p}'|^2, t) = \sqrt{\frac{E_\Lambda}{E_\Lambda - m_\Lambda} \mathcal{R}_-(|\mathbf{p}'|^2, t, t/2)}. \quad (33)$$

For $t \rightarrow \infty$, the quantities $R_\pm(|\mathbf{p}'|^2, t)$ become equal to the form factors $F_\pm(E_\Lambda)$ where $E_\Lambda = E_\Lambda(|\mathbf{p}'|^2)$.

Set	$N_s^3 \times N_t \times N_5$	am_5	$am_s^{(\text{sea})}$	$am_{u,d}^{(\text{sea})}$	a (fm)	$am_s^{(\text{val})}$	$am_{u,d}^{(\text{val})}$	$m_\pi^{(\text{vv})}$ (MeV)	$m_{\eta_s}^{(\text{vv})}$ (MeV)	N_{meas}
C14	$24^3 \times 64 \times 16$	1.8	0.04	0.005	0.1119(17)	0.04	0.001	245(4)	761(12)	2705
C24	$24^3 \times 64 \times 16$	1.8	0.04	0.005	0.1119(17)	0.04	0.002	270(4)	761(12)	2683
C54	$24^3 \times 64 \times 16$	1.8	0.04	0.005	0.1119(17)	0.04	0.005	336(5)	761(12)	2780
C53	$24^3 \times 64 \times 16$	1.8	0.04	0.005	0.1119(17)	0.03	0.005	336(5)	665(10)	1192
F23	$32^3 \times 64 \times 16$	1.8	0.03	0.004	0.0849(12)	0.03	0.002	227(3)	747(10)	1918
F43	$32^3 \times 64 \times 16$	1.8	0.03	0.004	0.0849(12)	0.03	0.004	295(4)	747(10)	1919
F63	$32^3 \times 64 \times 16$	1.8	0.03	0.006	0.0848(17)	0.03	0.006	352(7)	749(14)	2785

TABLE I. Parameters of the gauge field ensembles and quark propagators. Here, N_5 is the extent of the 5th dimension of the lattice, and am_5 is the domain-wall height [51]. The sea quark masses $am_q^{(\text{sea})}$ were used in the generation of the ensembles, and we use the valence-quark masses $am_q^{(\text{val})}$ when computing domain-wall propagators. The values for the lattice spacings, a , are taken from Ref. [60]. We denote the valence pion masses by $m_\pi^{(\text{vv})}$, and $m_{\eta_s}^{(\text{vv})}$ is defined as the mass of the pseudoscalar meson with valence strange-antistrange quarks, but without any disconnected contributions (we use $m_{\eta_s}^{(\text{vv})}$ to tune the strange-quark mass, using the approach of Ref. [61]). Finally, N_{meas} is the number of light/strange domain-wall propagator pairs computed on each ensemble.

a (fm)	$U(m_b, a^{-1})$	u_0	\mathcal{Z}	$c_\Gamma^{(m_s a)}$	$c_\Gamma^{(p_s a)}$
0.112	1.09964	0.875789	0.9383	$-0.1660 G_\Gamma$	$-0.1374 G_\Gamma$
0.085	1.06213	0.885778	0.9526	$-0.1482 G_\Gamma$	$-0.1294 G_\Gamma$

TABLE II. Renormalization parameters for the matching of LHQET to HQET in the $\overline{\text{MS}}$ scheme, from Ref. [56]. Here, G_Γ is defined by $\gamma^0 \Gamma \gamma^0 = G_\Gamma \Gamma$, so that $G_\Gamma = +1$ if Γ commutes with γ^0 , and $G_\Gamma = -1$ if Γ anticommutes with γ^0 .

B. Lattice parameters

The details of the domain-wall/Iwasaki gauge field ensembles generated by the RBC/UKQCD collaboration can be found in Ref. [51]. In Table I, we summarize the main properties of the subset of ensembles used here, as well as some parameters of the domain-wall propagators that we computed on them. There are ensembles with two different lattice spacings $a \approx 0.11$ fm and $a \approx 0.085$ fm, with lattice dimensions of $24^3 \times 64$ and $32^3 \times 64$, respectively, so that the spatial box size is $L \approx 2.7$ fm in both cases. We will refer to these two lattice spacings as “coarse” and “fine”. At the coarse lattice spacing, we use only one ensemble with the lightest available up/down sea-quark masses. At the fine lattice spacing, we use two different ensembles.

In order to construct the correlation functions discussed in Sec. III A, we require domain-wall propagators with Gaussian-smeared sources at (x_0, \mathbf{x}) , and with masses corresponding to the strange quark as well as the (degenerate) up/down quarks. As shown in Table I, we have seven different combinations of parameters, which we denote as C14, C24, C54, C53, F23, F43, F63 (where C, F stand for “coarse” and “fine”, and the two digits indicate the light and strange valence quark masses). In four of these combinations, the valence-quark masses are chosen to be lighter than the sea-quark masses (“partially quenched”), while the other three combinations have valence-quark masses equal to the sea-quark masses (unitary case). On each gauge configuration, we use $\mathcal{O}(10)$ source locations (x_0, \mathbf{x}) to increase statistics. The resulting total numbers of “measurements”, N_{meas} , are listed in Table I. On each configuration, we average the correlators over the source locations prior to further analysis.

In the static heavy-quark action, we use gauge links with one level of HYP smearing with the parameters $(\alpha_1, \alpha_2, \alpha_3) = (1.0, 1.0, 0.5)$ as introduced in Ref. [62]. The numerical values of the matching coefficients needed for the current (11) are taken from Ref. [56] and are given in Table II for the choice of HYP smearing parameters used here.

C. Results for \mathcal{R}_+ and \mathcal{R}_-

At the coarse lattice spacing, we computed the three-point functions (18), (19) for the source-sink separations $t/a = 4, 5, \dots, 15$, and at the fine lattice spacing for $t/a = 5, 6, \dots, 20$. We computed these three-point functions for lattice momenta \mathbf{p}' with $0 \leq |\mathbf{p}'|^2 \leq 9 \cdot (2\pi)^2/L^2$. We then constructed the quantities (27) and (28) using statistical bootstrap with 1000 samples. When performing the momentum direction average for the largest momentum $|\mathbf{p}'|^2 = 9 \cdot (2\pi)^2/L^2$, we used only $\mathbf{p}' = (2, 2, 1) \cdot 2\pi/L$ and lattice symmetries applied to that (for $|\mathbf{p}'|^2 < 9 \cdot (2\pi)^2/L^2$, all

possible \mathbf{p}' with the same magnitude are related by cubic rotations and reflections, and we average over all of them). Examples of numerical results for the quantities $\mathcal{R}_{\pm}(|\mathbf{p}'|^2, t, t')$ defined in Sec. III A are shown in Figs. 2-5. Except in the immediate neighborhood of $t' = 0$ and $t' = t$, the results for $\mathcal{R}_{\pm}(|\mathbf{p}'|^2, t, t')$ show only a weak dependence on the current-insertion time t' . However, a significant dependence on the source-sink separation t is seen, in particular for \mathcal{R}_{-} . Consequently, we need to extrapolate the results to infinite source-sink separation in order to remove the excited-state contamination. We perform these extrapolations for $R_{\pm}(|\mathbf{p}'|^2, t)$ [defined in Eqs. (32), (33)], as discussed in Sec. III E.

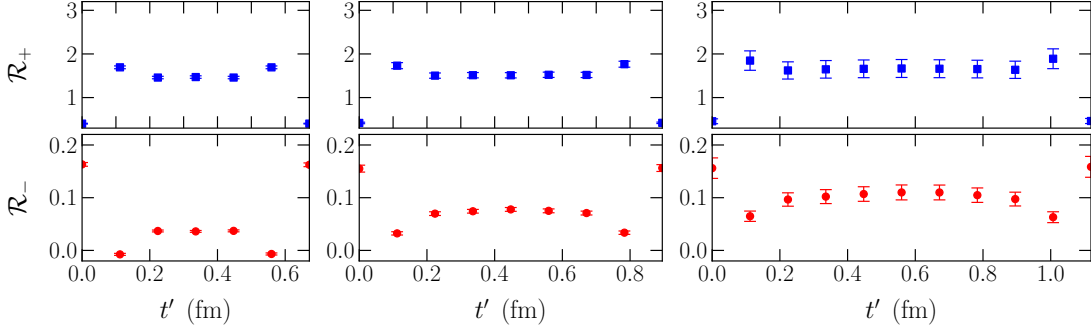


FIG. 2. Numerical results for $\mathcal{R}_{\pm}(|\mathbf{p}'|^2, t, t')$ at $|\mathbf{p}'|^2 = 1 \cdot (2\pi/L)^2$ from the C54 data set ($a = 0.112$ fm, $am_s^{(\text{val})} = 0.04$, $am_{u,d}^{(\text{val})} = 0.005$). The source-sink separations shown here are (from left to right) $t/a = 6, 8, 10$.

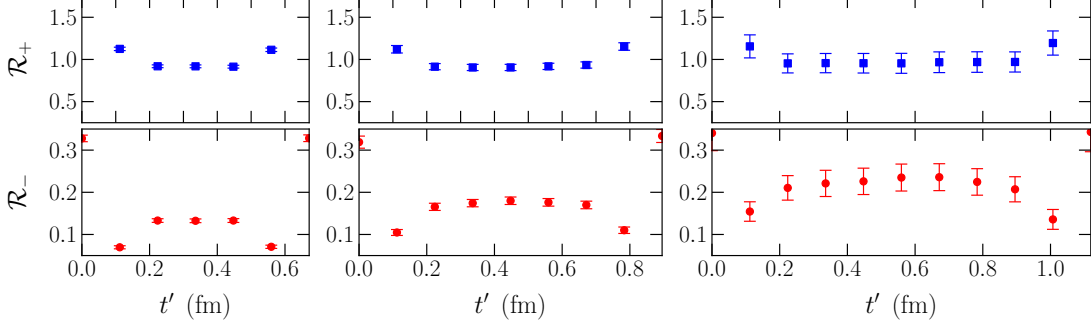


FIG. 3. Like Fig. 2, but at $|\mathbf{p}'|^2 = 4 \cdot (2\pi/L)^2$.

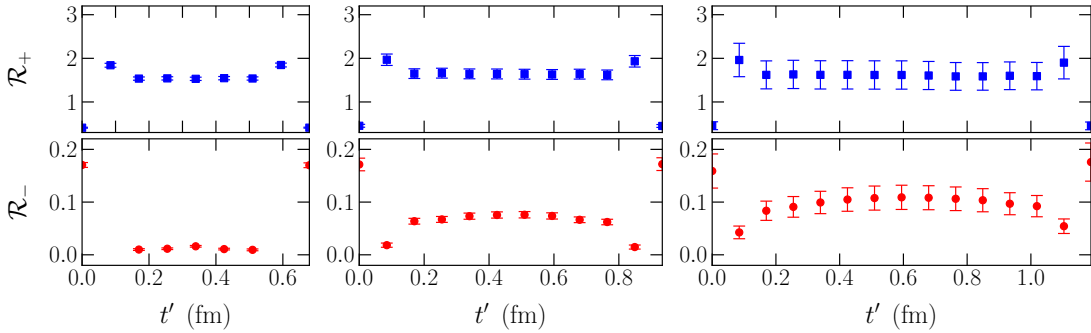


FIG. 4. Numerical results for $\mathcal{R}_{\pm}(|\mathbf{p}'|^2, t, t')$ at $|\mathbf{p}'|^2 = 1 \cdot (2\pi/L)^2$ from the F43 data set ($a = 0.085$ fm, $am_s^{(\text{val})} = 0.03$, $am_{u,d}^{(\text{val})} = 0.004$). The source-sink separations shown here are (from left to right) $t/a = 8, 11, 14$.

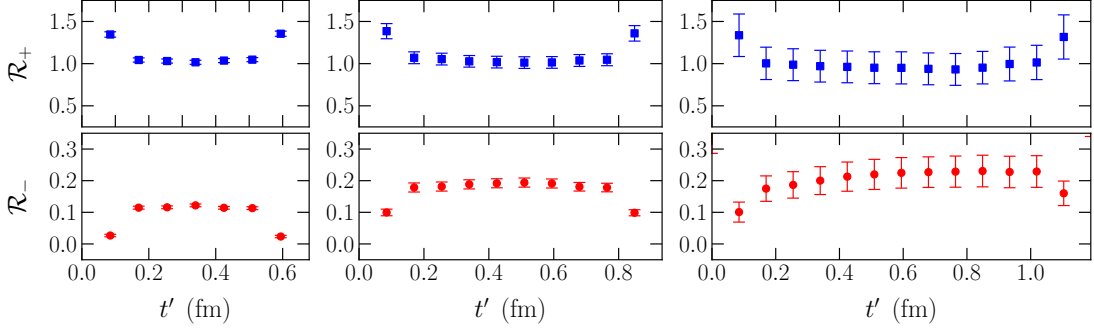


FIG. 5. Like Fig. 4, but at $|\mathbf{p}'|^2 = 4 \cdot (2\pi/L)^2$.

D. Fitting the Λ two-point functions

In order to compute the quantities $R_{\pm}(|\mathbf{p}'|^2, t)$, which were defined in Eqs. (32), (33), we use the energy $E_{\Lambda}(|\mathbf{p}'|^2)$ and mass $m_{\Lambda} = E_{\Lambda}(0)$ of the Λ baryon computed on the lattice for the same data set. To this end, we average the two-point function $\text{Tr}[C^{(2,\Lambda,\text{av})}(\mathbf{p}', t)]$ over momenta \mathbf{p}' with the same $|\mathbf{p}'|^2$, and perform correlated fits of the form $A e^{-E_{\Lambda} t}$ for sufficiently large t so that the excited-state contamination in the fitted E_{Λ} is negligible compared to the statistical uncertainty. To give an idea of the signal quality, we show the effective energy $(aE_{\Lambda})_{\text{eff}} = \ln[C(t)/C(t+a)]$ for selected momenta and two data sets in Fig. 6. The complete fit results for aE_{Λ} are listed in Table III. When computing $R_{\pm}(|\mathbf{p}'|^2, t)$ via Eqs. (32), (33), we used bootstrap to fully take into account the correlations between E_{Λ} , m_{Λ} , and $\mathcal{R}_{\pm}(|\mathbf{p}'|^2, t, t/2)$.

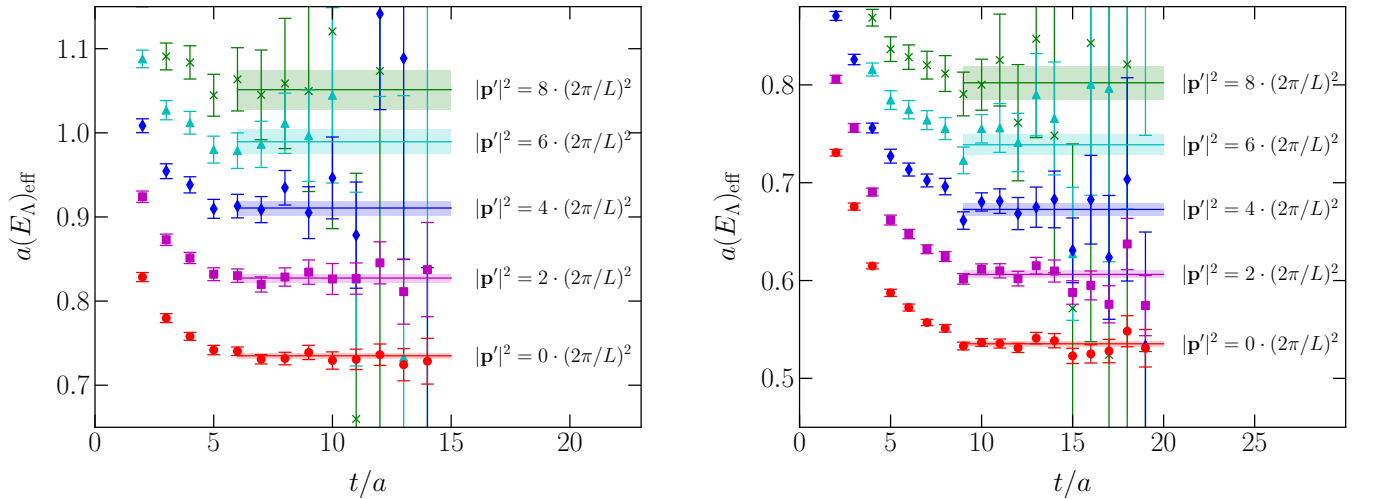


FIG. 6. Effective-energy plots for the Λ two-point functions at selected momenta. The shaded bands indicate the energies extracted from exponential fits of the two-point functions, as well as the t -range used for these fits. Left panel: $a = 0.112$ fm, $am_s^{(\text{val})} = 0.04$, $am_{u,d}^{(\text{val})} = 0.005$; right panel: $a = 0.085$ fm, $am_s^{(\text{val})} = 0.03$, $am_{u,d}^{(\text{val})} = 0.004$.

$ \mathbf{p}' ^2/(2\pi/L)^2$	C14	C24	C54	C53	F23	F43	F63
0	0.7046(41)	0.7135(45)	0.7350(34)	0.7150(42)	0.5191(41)	0.5353(29)	0.5540(17)
1	0.7542(46)	0.7613(53)	0.7821(40)	0.7653(49)	0.5575(46)	0.5717(32)	0.5894(19)
2	0.8027(58)	0.8061(69)	0.8274(52)	0.8151(62)	0.5931(53)	0.6062(38)	0.6240(24)
3	0.8460(76)	0.8495(97)	0.8709(69)	0.8612(84)	0.6288(67)	0.6422(50)	0.6568(31)
4	0.889(10)	0.896(11)	0.9106(87)	0.892(11)	0.6652(89)	0.6727(66)	0.6892(43)
5	0.921(11)	0.929(13)	0.948(11)	0.928(13)	0.695(10)	0.7033(79)	0.7201(52)
6	0.954(16)	0.965(19)	0.989(14)	0.966(17)	0.730(13)	0.739(10)	0.7479(64)
8	1.006(27)	1.021(31)	1.051(24)	1.014(30)	0.800(23)	0.802(17)	0.804(11)
9	1.033(35)	1.066(45)	1.087(32)	1.058(40)	0.839(30)	0.837(21)	0.822(14)

TABLE III. Fit results for $aE_\Lambda(|\mathbf{p}'|^2)$ from the different data sets (see Table I).

E. Extrapolation of R_+ and R_- to infinite source-sink separation

Using the methods outlined in the previous sections, we have obtained numerical results for $R_\pm(|\mathbf{p}'|^2, t)$ for multiple momenta $|\mathbf{p}'|^2$, for a wide range of source-sink separations t , and for seven different combinations of quark masses and lattice spacings. The next step is to compute the ground-state form factors F_\pm by extrapolating R_\pm to infinite source-sink separation. In the following, we use the notation $R_\pm^{i,n}(t)$, where $i = \text{C14, C24, ..., F63}$ labels the data set (see Table I), and $n = 0, 1, 2, 3, 4, 5, 6, 8, 9$ labels the momentum of the Λ , writing $|\mathbf{p}'|^2 = n \cdot (2\pi)^2/L^2$.

At zero momentum, we can only compute R_+ because \mathcal{R}_- vanishes for $E_\Lambda = m_\Lambda$ [see Eq. (30)]. Results for $R_+^{i,0}(t)$ from the two data sets $i = \text{C54, F43}$ are plotted in Fig. 7 as a function of the source-sink separation t . Remarkably, no significant t -dependence is found in this quantity, allowing constant fits of the form

$$R_+^{i,0}(t) = F_+^{i,0}, \quad (34)$$

which are also shown in Fig. 7. The fits fully take into account correlations and have $\chi^2/\text{dof} < 1$, showing that there is indeed no evidence for deviation from a constant. Note that R_+ can be obtained from the vector current $\bar{s}\gamma^0 b$ (in our calculation we have replaced γ^0 by 1 because $\gamma^0 Q = Q$ for static heavy quarks). In relativistic QCD, neglecting mass effects, charge conservation would then prevent any t -dependence at zero momentum, because excited states have the same charge as ground states. It appears that some remnant of this symmetry also remains in our case.

At non-zero Λ -momentum, both R_+ and R_- can be extracted, and significant t -dependence is seen. To extract the ground-state contributions F_+ and F_- , we perform fits including an exponential correction term that describes the

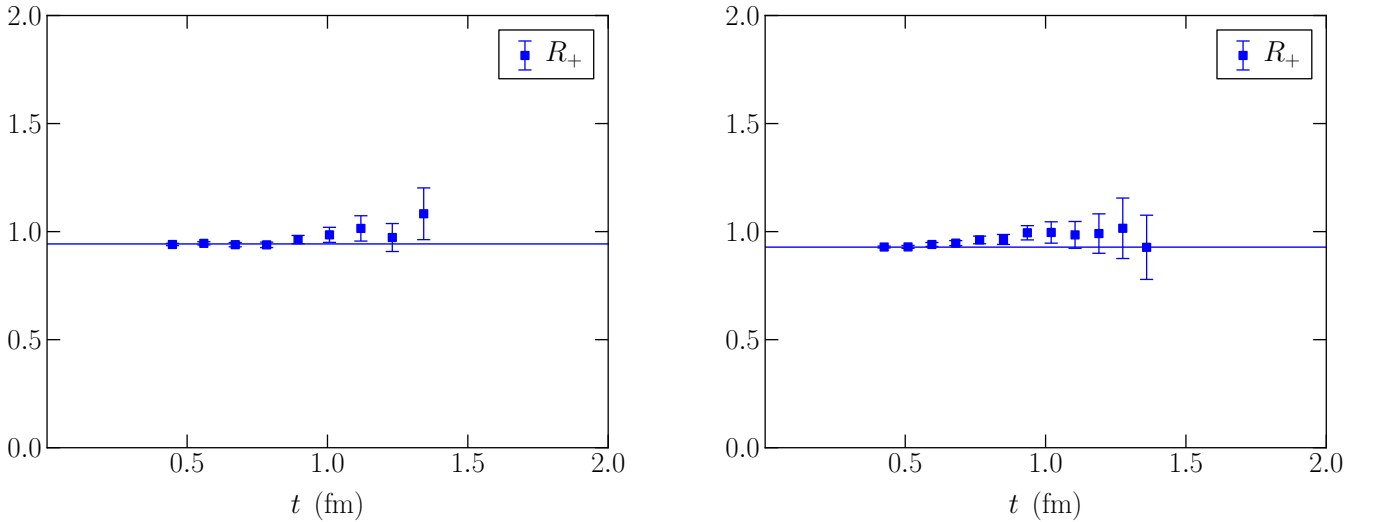


FIG. 7. Constant fits to the t -dependence of $R_+(t)$ at $|\mathbf{p}'|^2 = 0$. Left panel: $a = 0.112$ fm, $am_s^{(\text{val})} = 0.04$, $am_{u,d}^{(\text{val})} = 0.005$; right panel: $a = 0.085$ fm, $am_s^{(\text{val})} = 0.03$, $am_{u,d}^{(\text{val})} = 0.004$. The fits have χ^2/dof values of 0.92 and 0.78, respectively.

leading effects of excited states,

$$R_{\pm}^{i,n}(t) = F_{\pm}^{i,n} + A_{\pm}^{i,n} \exp[-\delta_{\pm}^{i,n} t], \quad (35)$$

where $F_{\pm}^{i,n}$, $A_{\pm}^{i,n}$, and $\delta_{\pm}^{i,n}$ are the fit parameters, which explicitly depend on the data set i and the momentum n . Because the energy gaps $\delta_{\pm}^{i,n}$ are positive by definition, we write

$$\delta_{\pm}^{i,n}/(1 \text{ GeV}) = \exp(l_{\pm}^{i,n}), \quad (36)$$

and use $l_{\pm}^{i,n}$ instead of $\delta_{\pm}^{i,n}$ as the fit parameters. The fits using Eq. (36) are performed separately for each momentum n , but simultaneously for the different data sets i . Note that the size of the momentum unit, $(2\pi)/L$ (in GeV), is the same at the coarse and fine lattice spacings within uncertainties, because the box sizes (in physical units) are equal within uncertainties. Performing the fits simultaneously for the different data sets at the same momentum allows us to use the prior knowledge that the hadron spectrum does not change dramatically when the lattice spacing or quark masses are varied by small amounts. To this end, we augment the χ^2 function used to perform the fits to Eq. (35) as follows:

$$\begin{aligned} \chi^2 \rightarrow \chi^2 &+ \frac{(l_{\pm}^{C14,n} - l_{\pm}^{C24,n})^2}{[\sigma_m^{C14,C24}]^2} + \frac{(l_{\pm}^{C24,n} - l_{\pm}^{C54,n})^2}{[\sigma_m^{C24,C54}]^2} + \frac{(l_{\pm}^{C54,n} - l_{\pm}^{C53,n})^2}{[\sigma_m^{C54,C53}]^2} \\ &+ \frac{(l_{\pm}^{F23,n} - l_{\pm}^{F43,n})^2}{[\sigma_m^{F23,F43}]^2} + \frac{(l_{\pm}^{F43,n} - l_{\pm}^{F63,n})^2}{[\sigma_m^{F43,F63}]^2} + \frac{(l_{\pm}^{C54,n} - l_{\pm}^{F63,n})^2}{[\sigma_m^{C54,F63}]^2 + \sigma_a^2}, \end{aligned} \quad (37)$$

where

$$[\sigma_m^{i,j}]^2 = w_m^2 [(m_{\pi}^i)^2 - (m_{\pi}^j)^2]^2 + w_m^2 [(m_{\eta_s}^i)^2 - (m_{\eta_s}^j)^2]^2, \quad (38)$$

with $w_m = 4 \text{ GeV}^{-2}$, and $\sigma_a = 0.1$. With these parameters, Eq. (37) implements the constraint that the energy gaps, at given Λ -momentum n , should not change by more than 10% when going from the fine to the coarse lattice spacing, and not more than 400% times the change in m_{π}^2 or $m_{\eta_s}^2$ (in GeV^2). Note that absolute variations of $l_{\pm}^{i,n}$ translate to relative variations of $\delta_{\pm}^{i,n}$, because $d[\exp(l_{\pm}^{i,n})]/\exp(l_{\pm}^{i,n}) = dl_{\pm}^{i,n}$.

Example fits of $R_{\pm}^{i,n}(t)$ using Eq. (35) are shown in Fig. 8. The fits are fully correlated, using covariance matrices computed from the bootstrap ensembles for $R_{\pm}^{i,n}(t)$. Note that the excited-state contribution in R_+ , which is negligible at $\mathbf{p}' = 0$ (cf. Fig. 7), gradually increases with the momentum. In contrast, R_- shows the strongest excited-state overlap at the smallest momentum, and this overlap decreases as the momentum increases. The excited-state overlap is slightly stronger at the fine lattice spacing when compared to the coarse lattice spacing. This is expected because the quark smearing width in the baryon operators was different for the two lattice spacings (we used the same width in lattice units). We only computed the correlators for $t/a \geq 4$ at the coarse lattice spacing and $t/a \geq 5$ at the fine lattice spacing. At the fine lattice spacing, it was necessary to exclude the points with $t/a < 8$ from the fits to R_- . Once these points were excluded, all fits had $\chi^2/\text{dof} \approx 1.0$. Given the limited time range and the limited statistical precision of the available data, it was not possible (and not necessary) to perform fits with more than one exponential. As a check, we have also performed fits without the constraints (37), which give consistent results but are less stable.

The fitted values of the energy gap parameters, $\delta_{\pm}^{i,n} = \exp(l_{\pm}^{i,n}) \cdot (1 \text{ GeV})$, are shown as a function of the Λ -momentum for one ensemble in Fig. 9 (left panel). Within uncertainties, we find that

$$\delta_+^{i,n} = \delta_-^{i,n}, \quad (39)$$

for all data sets i and momenta n . The energy spectrum is a property of the QCD Hamiltonian and is independent of the correlation function considered, so the result (39) is not surprising. However, one possible situation in which $\delta_+^{i,n}$ and $\delta_-^{i,n}$ would be different is when an excited state has negligible overlap in R_+ but significant overlap in R_- (or vice versa). Furthermore, by using only a single exponential, we may be effectively averaging over multiple excited states which we cannot resolve individually, but which may appear with different sets of weights in R_+ and R_- . Having said that, the values of $\delta_+^{i,n}$ and $\delta_-^{i,n}$ from our fits are in complete agreement and it is evident that the separate parameters $\delta_+^{i,n}$ and $\delta_-^{i,n}$ may be replaced by a single parameter $\delta^{i,n}$. Thus, we performed new, coupled fits of R_+ and R_- of the form

$$R_{\pm}^{i,n}(t) = F_{\pm}^{i,n} + A_{\pm}^{i,n} \exp[-\delta^{i,n} t], \quad (40)$$

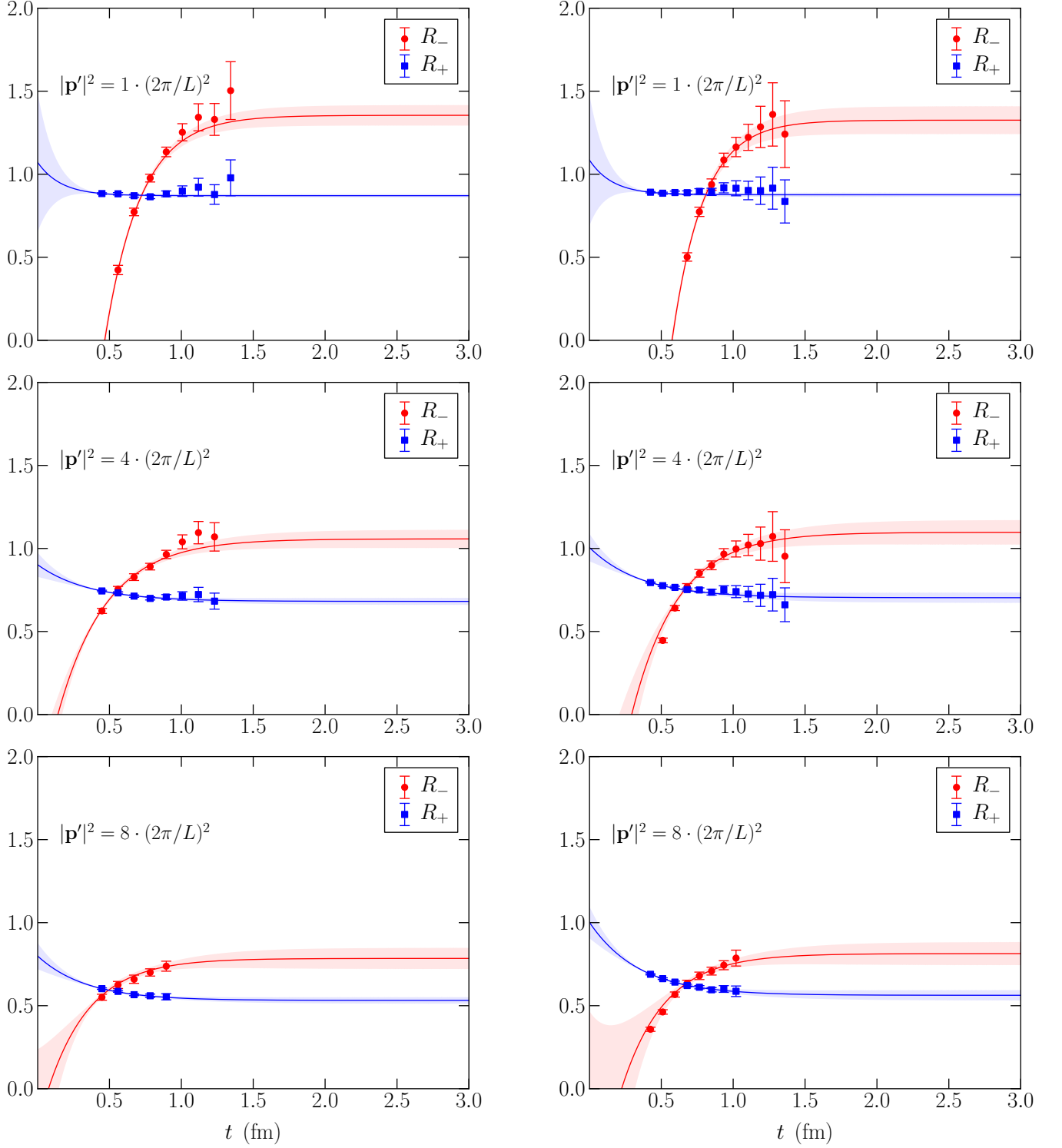


FIG. 8. Fits of the t -dependence of $R_{\pm}(t)$ using Eq. (35). Left panels: $a = 0.112$ fm, $am_s^{(\text{val})} = 0.04$, $am_{u,d}^{(\text{val})} = 0.005$; right panels: $a = 0.085$ fm, $am_s^{(\text{val})} = 0.03$, $am_{u,d}^{(\text{val})} = 0.004$. At the fine lattice spacing, only the points with $t > 0.6$ fm are included in the fit of R_- . The maximum values of t for the data were limited by statistical noise in the two-point and three-point functions; for t larger than the right-most points in the plots, the statistical fluctuations were too large to compute the square roots in Eqs. (32) and (33).

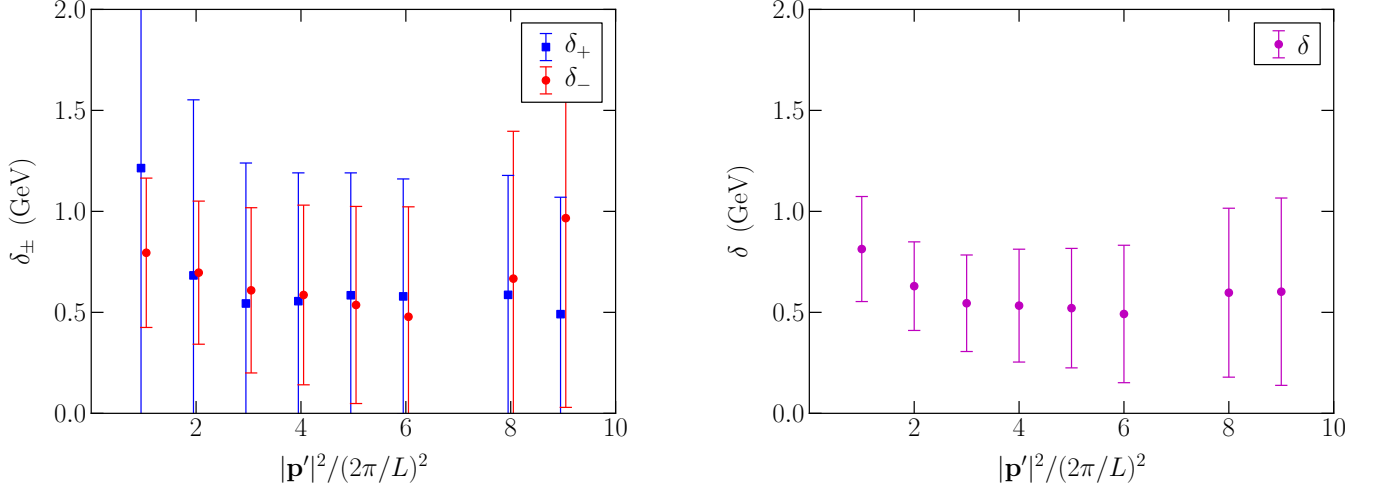


FIG. 9. Left: results for the energy gap parameters from separate fits of R_+ and R_- using Eq. (35). The points are offset horizontally for clarity. Right: results for the energy gap parameters from coupled fits of R_+ and R_- using Eq. (40). The data shown here are for $a = 0.112$ fm, $am_s^{(\text{val})} = 0.04$, $am_{u,d}^{(\text{val})} = 0.005$.

$ \mathbf{p}' ^2/(2\pi/L)^2$	C14	C24	C54	C53	F23	F43	F63
0	0.9416(56)	0.9443(66)	0.9430(59)	0.9390(71)	0.9320(58)	0.9281(49)	0.920(13)
1	0.868(14)	0.874(27)	0.871(23)	0.873(26)	0.878(33)	0.876(18)	0.807(25)
2	0.785(15)	0.786(34)	0.788(27)	0.791(25)	0.823(25)	0.818(14)	0.738(28)
3	0.717(15)	0.705(36)	0.715(28)	0.723(24)	0.770(26)	0.763(14)	0.680(28)
4	0.671(15)	0.669(26)	0.672(22)	0.668(17)	0.697(32)	0.698(15)	0.633(28)
5	0.618(15)	0.612(26)	0.621(21)	0.622(15)	0.667(27)	0.664(16)	0.587(27)
6	0.586(16)	0.580(20)	0.576(20)	0.577(15)	0.625(30)	0.621(19)	0.554(29)
8	0.537(14)	0.545(16)	0.532(13)	0.516(24)	0.569(27)	0.563(22)	0.507(39)
9	0.508(17)	0.516(16)	0.502(15)	0.491(26)	0.546(31)	0.536(28)	0.484(40)

TABLE IV. Results for F_+ from the different data sets (see Table I). The uncertainties presented combine statistical and systematic fitting uncertainties in quadrature.

with energy gap parameters $\delta^{i,n} = \exp(l^{i,n}) \cdot (1 \text{ GeV})$ that are shared between R_+ and R_- . The results for $\delta^{i,n}$ from the coupled fits are shown in the right panel of Fig. 9. We note that the coupled fits had values of χ^2/dof that were as good or better than the values from the separate fits, confirming that the assumption (39) is justified.

The results for the extracted ground-state form factors $F_{\pm}^{i,n}$ from separate and coupled fits are compared in Fig. 10. As can be seen there, the results are consistent with each other, but the coupled fits with shared energy gap parameters give significantly smaller uncertainties, in particular for F_- . Therefore, we use the results from the coupled fits in our further analysis.

To estimate the systematic uncertainty resulting from the choice of the fit range in t , we computed the changes in $F_{\pm}^{i,n}$ when increasing t_{\min} by one unit simultaneously for all data sets, thereby removing the points with the most contamination from additional higher excited states. As can be seen in Fig. 11, the resulting change in the fitted $F_{\pm}^{i,n}$ is small, and in most cases consistent with zero. Nevertheless, we add this shift in quadrature to the original statistical uncertainty of $F_{\pm}^{i,n}$. The final results for $F_{\pm}^{i,n}$, including this systematic uncertainty, are given in Tables IV and V. For convenience, we also provide results for $F_1^{i,n} = (F_+^{i,n} + F_-^{i,n})/2$ and $F_2^{i,n} = (F_+^{i,n} - F_-^{i,n})/2$, computed using bootstrap to take into account the correlations between $F_+^{i,n}$ and $F_-^{i,n}$, in Tables VI and VII.

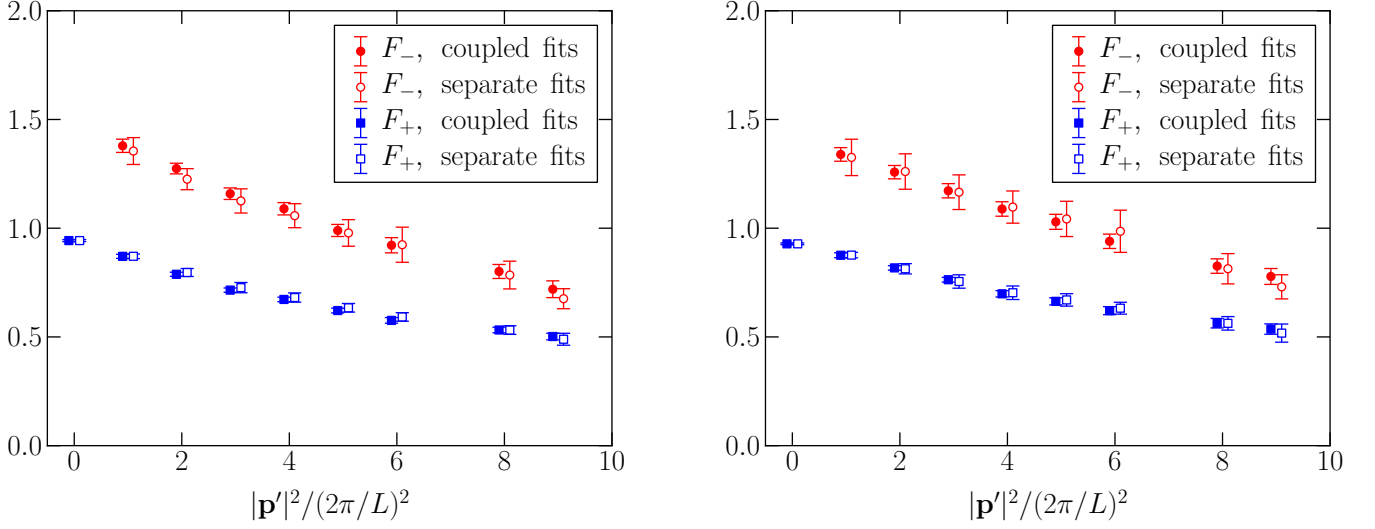


FIG. 10. Fit results for the ground-state contributions F_+ and F_- from separate fits of R_+ and R_- using Eq. (35) vs results from coupled fits using Eq. (40). Left panel: $a = 0.112$ fm, $am_s^{(\text{val})} = 0.04$, $am_{u,d}^{(\text{val})} = 0.005$; right panel: $a = 0.085$ fm, $am_s^{(\text{val})} = 0.03$, $am_{u,d}^{(\text{val})} = 0.004$. The points are offset horizontally for clarity.

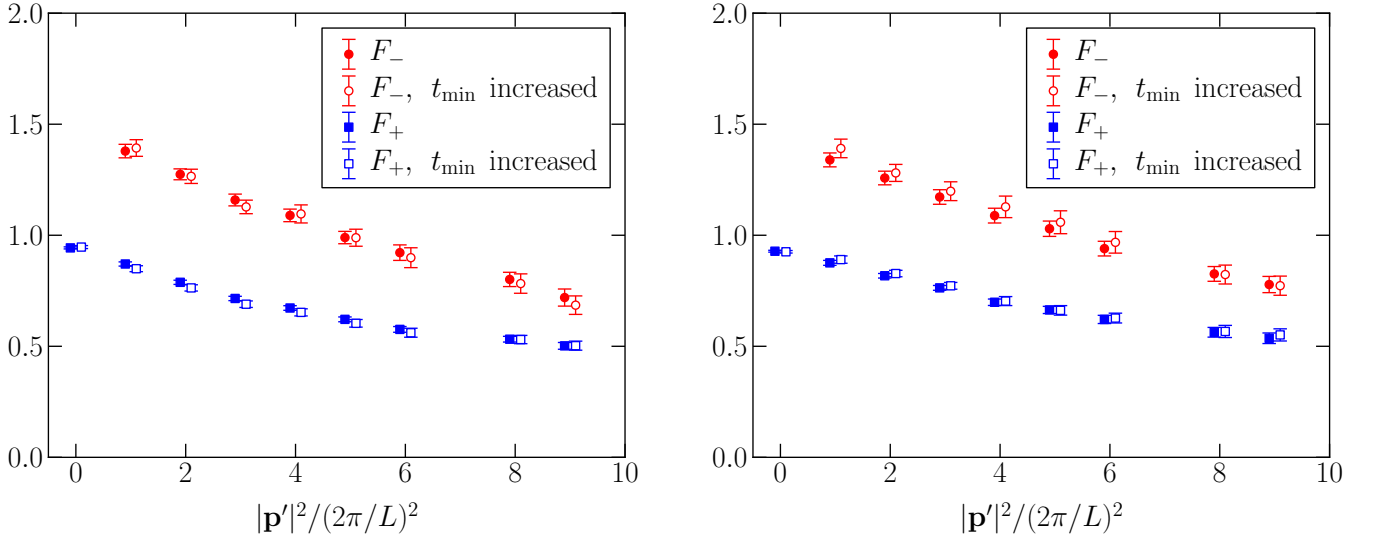


FIG. 11. Fit results for the ground-state contributions F_+ and F_- from coupled fits of R_+ and R_- using Eq. (40): effect of increasing all t_{\min} values by one unit. Left panel: $a = 0.112$ fm, $am_s^{(\text{val})} = 0.04$, $am_{u,d}^{(\text{val})} = 0.005$; right panel: $a = 0.085$ fm, $am_s^{(\text{val})} = 0.03$, $am_{u,d}^{(\text{val})} = 0.004$. The points are offset horizontally for clarity.

$ \mathbf{p}' ^2/(2\pi/L)^2$	C14	C24	C54	C53	F23	F43	F63
1	1.355(53)	1.422(52)	1.379(33)	1.346(41)	1.352(57)	1.339(60)	1.296(51)
2	1.233(58)	1.278(36)	1.274(26)	1.230(35)	1.241(45)	1.258(38)	1.185(49)
3	1.143(36)	1.163(43)	1.159(41)	1.135(72)	1.183(52)	1.172(42)	1.094(47)
4	1.032(51)	1.084(40)	1.089(29)	1.071(44)	1.094(81)	1.088(52)	1.004(49)
5	0.973(34)	0.990(35)	0.990(28)	0.967(49)	1.035(73)	1.029(45)	0.928(47)
6	0.904(35)	0.905(43)	0.922(42)	0.907(65)	0.938(82)	0.940(44)	0.872(45)
8	0.752(33)	0.790(42)	0.801(37)	0.820(74)	0.805(58)	0.826(33)	0.742(48)
9	0.700(43)	0.706(51)	0.719(52)	0.712(76)	0.748(58)	0.778(37)	0.707(41)

TABLE V. Results for F_- from the different data sets (see Table I). The uncertainties presented combine statistical and systematic fitting uncertainties in quadrature.

$ \mathbf{p}' ^2/(2\pi/L)^2$	C14	C24	C54	C53	F23	F43	F63
1	1.111(31)	1.148(32)	1.125(18)	1.110(23)	1.115(40)	1.107(38)	1.051(35)
2	1.009(35)	1.032(26)	1.031(23)	1.011(26)	1.032(30)	1.038(24)	0.961(37)
3	0.930(21)	0.934(35)	0.937(32)	0.929(46)	0.976(33)	0.968(25)	0.887(36)
4	0.852(29)	0.876(20)	0.881(17)	0.870(25)	0.895(50)	0.893(28)	0.818(35)
5	0.795(18)	0.801(22)	0.805(18)	0.795(27)	0.851(41)	0.846(22)	0.757(34)
6	0.745(19)	0.743(26)	0.749(26)	0.742(33)	0.782(48)	0.780(24)	0.713(34)
8	0.644(17)	0.667(24)	0.666(19)	0.668(31)	0.687(32)	0.695(17)	0.624(41)
9	0.604(23)	0.611(27)	0.611(24)	0.602(32)	0.647(35)	0.657(19)	0.595(35)

TABLE VI. Results for F_1 from the different data sets (see Table I). The uncertainties presented combine statistical and systematic fitting uncertainties in quadrature.

$ \mathbf{p}' ^2/(2\pi/L)^2$	C14	C24	C54	C53	F23	F43	F63
1	-0.244(23)	-0.274(26)	-0.254(23)	-0.236(25)	-0.237(23)	-0.232(23)	-0.244(19)
2	-0.224(25)	-0.246(23)	-0.243(14)	-0.220(16)	-0.209(21)	-0.220(16)	-0.224(16)
3	-0.213(17)	-0.229(20)	-0.222(13)	-0.206(27)	-0.207(24)	-0.205(19)	-0.207(15)
4	-0.181(24)	-0.208(27)	-0.209(19)	-0.202(22)	-0.199(35)	-0.195(26)	-0.186(18)
5	-0.177(19)	-0.189(21)	-0.184(17)	-0.173(24)	-0.184(37)	-0.183(26)	-0.171(18)
6	-0.159(20)	-0.163(21)	-0.173(20)	-0.165(34)	-0.157(38)	-0.159(24)	-0.159(17)
8	-0.108(19)	-0.123(21)	-0.135(21)	-0.152(46)	-0.118(32)	-0.131(22)	-0.118(16)
9	-0.096(23)	-0.095(27)	-0.109(29)	-0.111(47)	-0.101(30)	-0.121(27)	-0.111(20)

TABLE VII. Results for F_2 from the different data sets (see Table I). The uncertainties presented combine statistical and systematic fitting uncertainties in quadrature.

F. Chiral and continuum extrapolation of the form factors

The last step in our analysis of the lattice data is to fit the dependence of $F_{\pm}^{i,n}$ on the quark masses, the lattice spacing, and on E_{Λ} . The form of the dependence is unknown; low-energy effective field theory combining heavy-baryon chiral perturbation theory for the Λ sector and heavy-hadron chiral perturbation theory for the Λ_Q sector may be useful over some range of E_{Λ} , but not in the region with $|\mathbf{p}'| \gtrsim \Lambda_{\chi}$, where $\Lambda_{\chi} \sim 1$ GeV is the chiral symmetry-breaking scale. We therefore use a simple ansatz that fits our data well at the level of statistical precision that we have. In the following it is advantageous to express the form factors as functions of the energy difference $E_{\Lambda} - m_{\Lambda}$ instead of E_{Λ} , as this depends less on the quark masses. We find that this dependence can be described well using a dipole function of the form $F_{\pm} = N_{\pm}/(X_{\pm} + E_{\Lambda} - m_{\Lambda})^2$. We generalize this ansatz to allow for dependence on the light and strange quark masses, as well as the lattice spacing, in the following way:

$$F_{\pm}^{i,n} = \frac{N_{\pm}}{(X_{\pm}^i + E_{\Lambda}^{i,n} - m_{\Lambda}^i)^2} \cdot [1 + d_{\pm}(a^i E_{\Lambda}^{i,n})^2], \quad (41)$$

where the functions X_{\pm}^i are defined as

$$X_{\pm}^i = X_{\pm} + c_{l,\pm} \cdot [(m_{\pi}^i)^2 - (m_{\pi}^{\text{phys}})^2] + c_{s,\pm} \cdot [(m_{\eta_s}^i)^2 - (m_{\eta_s}^{\text{phys}})^2]. \quad (42)$$

As before, we use the notation where $i = \text{C14, C24, ..., F63}$ labels the data set (see Table I), and n labels the momentum of the Λ . The free fit parameters in Eq. (41) are N_{\pm} , X_{\pm} , d_{\pm} , $c_{l,\pm}$, and $c_{s,\pm}$. The dependence of the form factors on the light and strange quark masses is described by allowing X_{\pm}^i to depend linearly on $(m_{\pi}^i)^2$ and $(m_{\eta_s}^i)^2$, where m_{π}^i and $m_{\eta_s}^i$ are the valence π and η_s masses for each data set i , as given in Table I. We wrote Eq. (42) in terms of the differences between the lattice and physical masses for convenience, with $m_{\pi}^{\text{phys}} = 138$ MeV and $m_{\eta_s}^{\text{phys}} = 686$ MeV [61]. The leading dependence of the form factors on the lattice spacing is expected to be quadratic in a , owing to the chiral symmetry of the domain-wall action and the use of the order- a -improved current (11). Discretization errors are expected to grow as the momentum of the Λ increases. We therefore incorporate the a -dependence using the factor $[1 + d_{\pm}(a^i E_{\Lambda}^{i,n})^2]$ in Eq. (41).

In our fits, we take into account the correlations between the results for $F_{\pm}^{i,n}$ at different momenta n and different data sets i (in the case where the data sets correspond to the same underlying ensemble of gauge fields). The fits are performed independently for $F_{+}^{i,n}$ and $F_{-}^{i,n}$. To account for the uncertainties and correlations of the Λ baryon energies $E_{\Lambda}^{i,n}$ (including the masses $m_{\Lambda}^i = E_{\Lambda}^{i,0}$) in Eq. (41), we promote $E_{\Lambda}^{i,n}$ to additional parameters of the fit, and add the term $\sum_{i,n,i',n'} [\text{Cov}(E_{\Lambda})^{-1}]_{i,n,i',n'} (E_{\Lambda}^{i,n} - \bar{E}_{\Lambda}^{i,n})(E_{\Lambda}^{i',n'} - \bar{E}_{\Lambda}^{i',n'})$ to the χ^2 function, where $\bar{E}_{\Lambda}^{i,n}$ are the previous results from the fits to the two-point functions, and the energy correlation matrix $\text{Cov}(E_{\Lambda})$ was computed from the bootstrap ensemble of the two-point fit results. Using a similar term, we investigated the inclusion of the further correlations between the Λ energies and the form factor values $F_{\pm}^{i,n}$, but with the current level of statistics, such fits did not converge to a stable minimum of χ^2 .

The fits using Eq. (41) are visualized as a function of $E_{\Lambda} - m_{\Lambda}$ in Fig. 12. There, we show the results for $F_{\pm}^{i,n}$ from Tables IV and V, along with the fitted functions (41) evaluated at the corresponding lattice spacings a^i and pseudoscalar masses, m_{π}^i and $m_{\eta_s}^i$. The data are described well by the fitted functions (the F63 set fluctuates downward, but the overall values of χ^2/dof are smaller than 1). The bottom-right plot in Fig. 12 shows the fit functions evaluated in the continuum limit ($a = 0$) and for the physical values of the pseudoscalar masses. By construction, in this physical limit, Eq. (41) reduces to

$$F_{\pm} = \frac{N_{\pm}}{(X_{\pm} + E_{\Lambda} - m_{\Lambda})^2}, \quad (43)$$

which only depends on the parameters N_{\pm} and X_{\pm} . Our results for N_{\pm} and X_{\pm} are given in Table VIII. The results for the parameters describing the dependence on the quark masses and the lattice-spacing are $c_{l,+} = 0.094(32) \text{ GeV}^{-1}$, $c_{s,+} = -0.019(27) \text{ GeV}^{-1}$, $d_{+} = 0.027(27)$, $c_{l,-} = 0.04(20) \text{ GeV}^{-1}$, $c_{s,-} = -0.14(11) \text{ GeV}^{-1}$, and $d_{-} = -0.036(67)$, which are all very small and mostly consistent with zero.

Functions for the form factors F_1 and F_2 could be obtained from (43) by taking the linear combinations $F_1 = (F_{+} + F_{-})/2$ and $F_2 = (F_{+} - F_{-})/2$. However, because we use independent pole parameters X_{+} and X_{-} , these linear combinations are no longer of the simple dipole form. Alternatively, we can also perform new fits to the lattice data $F_1^{i,n} = (F_{+}^{i,n} + F_{-}^{i,n})/2$ and $F_2^{i,n} = (F_{+}^{i,n} - F_{-}^{i,n})/2$ using functions of the same form as in Eq. (41), but with new parameters labeled by the subscripts 1, 2 instead of +, -:

$$F_{1,2}^{i,n} = \frac{N_{1,2}}{(X_{1,2}^i + E_{\Lambda}^{i,n} - m_{\Lambda}^i)^2} \cdot [1 + d_{1,2}(a^i E_{\Lambda}^{i,n})^2]. \quad (44)$$

Parameter	Result
N_+	$3.188 \pm 0.268 \text{ GeV}^2$
X_+	$1.852 \pm 0.074 \text{ GeV}$
N_-	$4.124 \pm 0.750 \text{ GeV}^2$
X_-	$1.634 \pm 0.144 \text{ GeV}$

TABLE VIII. Fit results for N_{\pm} and X_{\pm} using Eq. (41). The covariances are $\text{Cov}(N_+, X_+) = 0.0198 \text{ GeV}^3$, $\text{Cov}(N_-, X_-) = 0.106 \text{ GeV}^3$. The results are renormalized in the $\overline{\text{MS}}$ scheme at $\mu = m_b$.

Parameter	Result
N_1	$3.975 \pm 0.576 \text{ GeV}^2$
X_1	$1.776 \pm 0.123 \text{ GeV}$
N_2	$-0.385 \pm 0.132 \text{ GeV}^2$
X_2	$1.156 \pm 0.200 \text{ GeV}$

TABLE IX. Fit results for $N_{1,2}$ and $X_{1,2}$ as discussed in the main text. The covariances are $\text{Cov}(N_1, X_1) = 0.0692 \text{ GeV}^3$, $\text{Cov}(N_2, X_2) = -0.0256 \text{ GeV}^3$. The results are renormalized in the $\overline{\text{MS}}$ scheme at $\mu = m_b$.

These fits are visualized in Fig. 13, and the resulting parameters $N_{1,2}$, $X_{1,2}$ are given in Table IX. In this case, the results for the other fit parameters were $c_{l,1} = 0.09(17) \text{ GeV}^{-1}$, $c_{s,1} = -0.067(94) \text{ GeV}^{-1}$, $d_1 = -0.049(53)$, $c_{l,2} = -0.06(38) \text{ GeV}^{-1}$, $c_{s,2} = -0.35(22) \text{ GeV}^{-1}$, and $d_2 = 0.00(15)$.

G. Estimates of systematic uncertainties

The remaining systematic uncertainties in our form factor results include missing higher-order renormalization corrections to the heavy-light current, finite-volume effects, chiral-extrapolation errors, and residual discretization errors. We discuss each of these below. Furthermore, for large $E_{\Lambda} - m_{\Lambda}$, where we do not have lattice data, our assumption of a dipole shape in Eqs. (41) and (44) introduces an unknown model-dependence. This is illustrated in Fig. 14), where we compare the dipole fits to monopole fits. However, we do not have confidence that this difference is a reliable estimate of a fitting form systematic uncertainty (or indeed that such a systematic uncertainty can be constructed) and so leave this to the judgment of the reader.

To estimate the systematic uncertainty due to missing higher-order renormalization corrections to the heavy-light current (11), we vary the scale μ in the matching coefficients $\mathcal{Z}(\mu)$, $c^{(msa)}(\mu)$, $c^{(psa)}(\mu)$, and in the renormalization-group running $U(m_b, \mu)$. We then recompute the ratios (32) and (33) with the modified current. Changing μ from a^{-1} to $2a^{-1}$ results in a 7% change of both R_+ and R_- at the coarse lattice spacing and a 6% change of both R_+ and R_- at the fine lattice spacing. These relative changes are nearly independent of the source-sink separation, the momentum, and the quark masses. Thus, we take the renormalization uncertainty in the final form factor results to be 6%.

Finite-volume effects in the lattice data are unknown (as in the chiral extrapolation, no low-energy effective theory exists to guide us over the full range of E_{Λ}), but are expected to be of order $\exp(-m_{\pi}L)$. The lowest pion mass used in our calculation is $m_{\pi} \approx 227 \text{ MeV}$, corresponding to $m_{\pi}L \approx 3.1$ and $\exp(-m_{\pi}L) \approx 0.04$. The average value of $\exp(-m_{\pi}L)$ for the different data sets (see Table I) is about 0.02. Given these values, we estimate the systematic uncertainty in our final results due to finite-volume effects to be 3%.

The chiral extrapolations of the form factors were performed quadratically in the valence pseudoscalar masses, i.e. linearly in the valence-quark masses, ignoring that some of the data were partially quenched and ignoring possible nonanalytic dependence on the quark masses. To study the effect of the quark-mass extrapolations, we perform new fits with either $c_{l,\pm}$ or $c_{s,\pm}$, or both, set to zero, and consider the changes in the extracted form factors F_+ and F_- (analogously also for F_1 and F_2). This corresponds to replacing the linear fits of the quark-mass dependence by constant fits. The resulting relative changes in F_+ , F_- , F_1 , and F_2 when setting $c_l = 0$ are below 1% throughout the kinematic range where we have lattice data; the biggest relative change (5%) is seen in F_2 at zero recoil when setting $c_s = 0$. However, all of the changes are consistent with zero within statistical uncertainties.

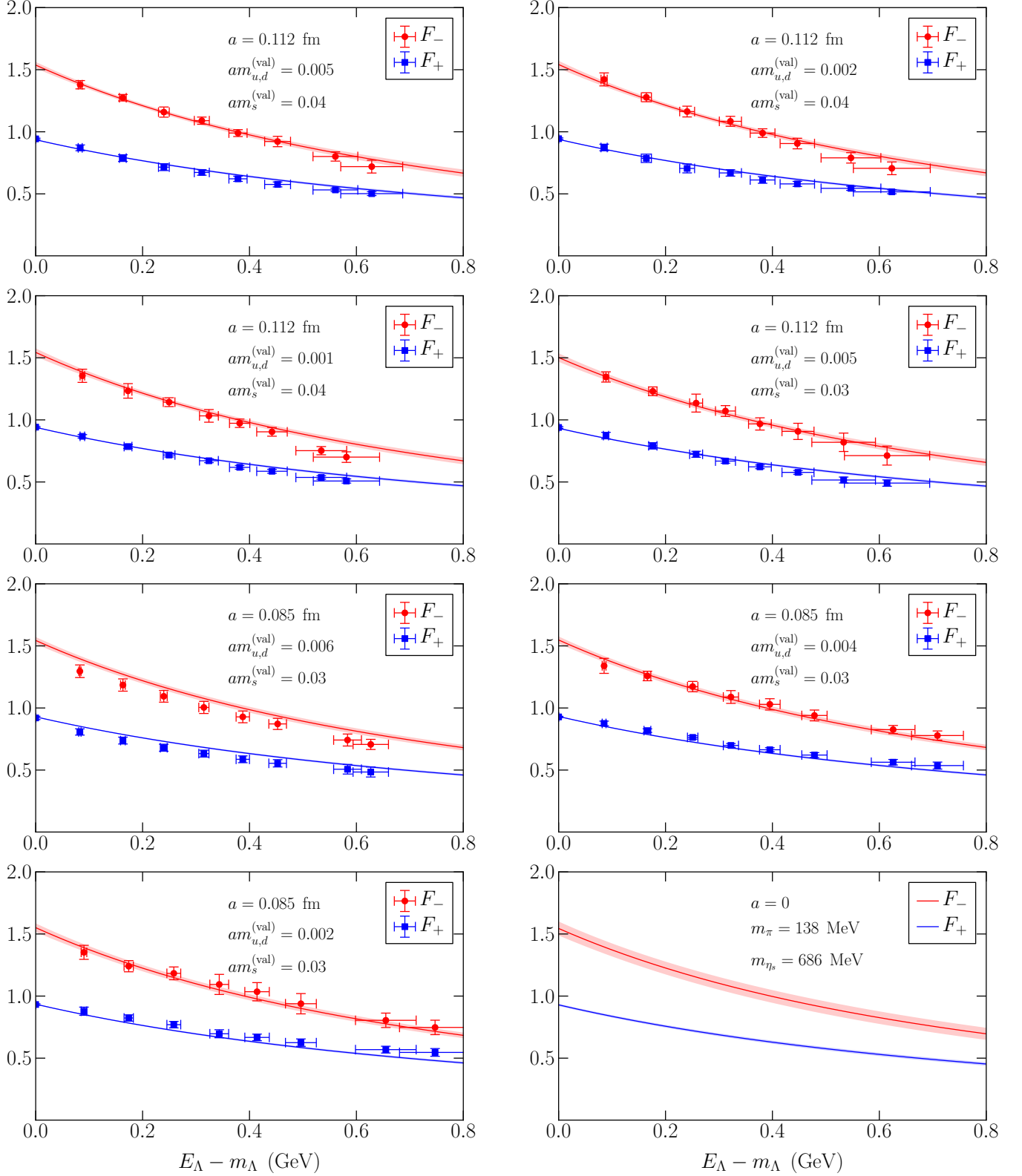


FIG. 12. Fits of the form factor data for F_+ and F_- using Eq. (41). The fit of F_+ has $\chi^2/\text{dof} = 0.84$, and the fit of F_- has $\chi^2/\text{dof} = 0.72$. The lowest right plot shows the continuum form factors for the physical light- and strange quark masses.

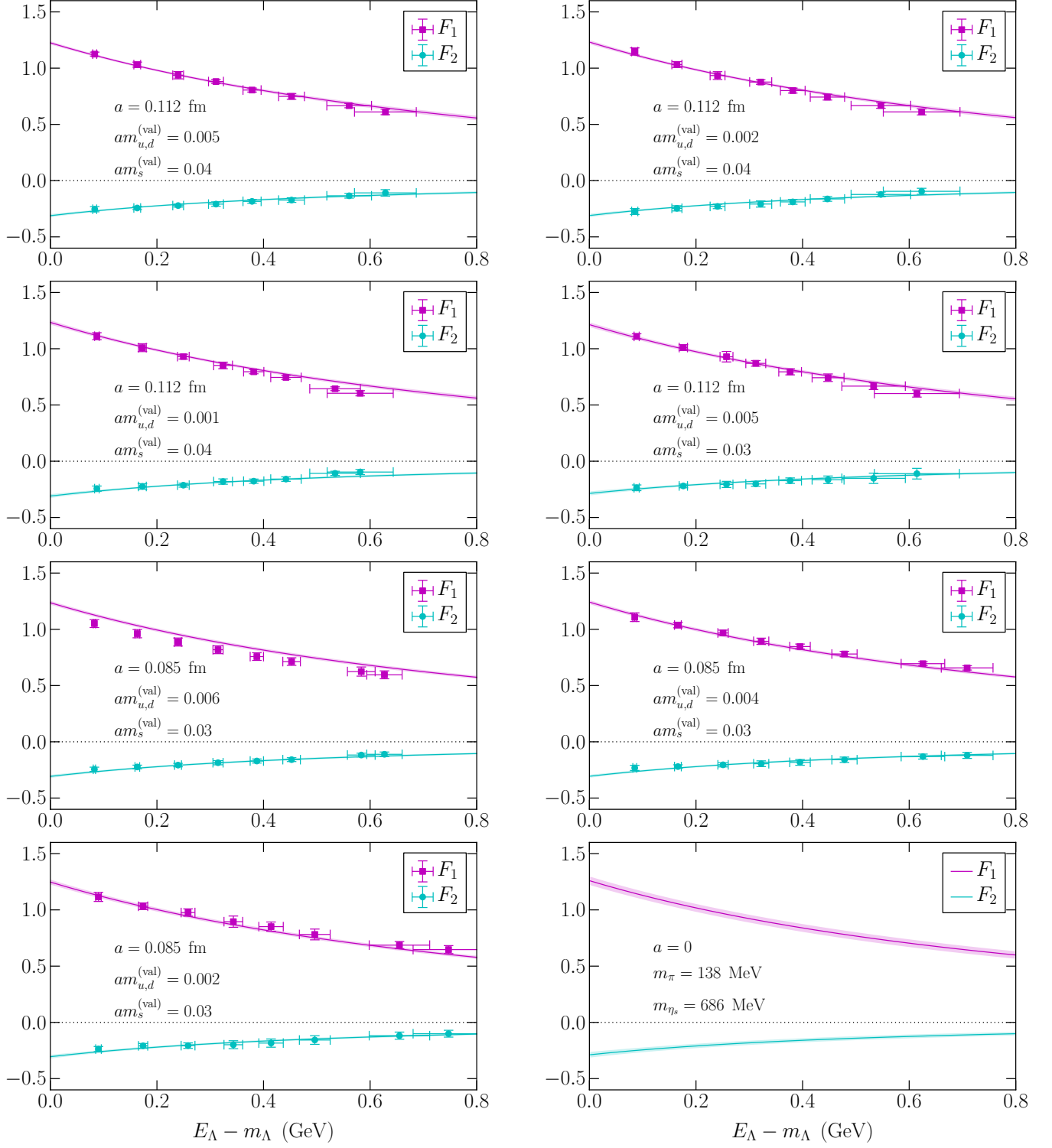


FIG. 13. Fits of the form factor data for F_1 and F_2 using Eq. (44). The fit of F_1 has $\chi^2/\text{dof} = 0.59$, and the fit of F_2 has $\chi^2/\text{dof} = 0.85$. The lowest right plot shows the continuum form factors for the physical light- and strange quark masses.

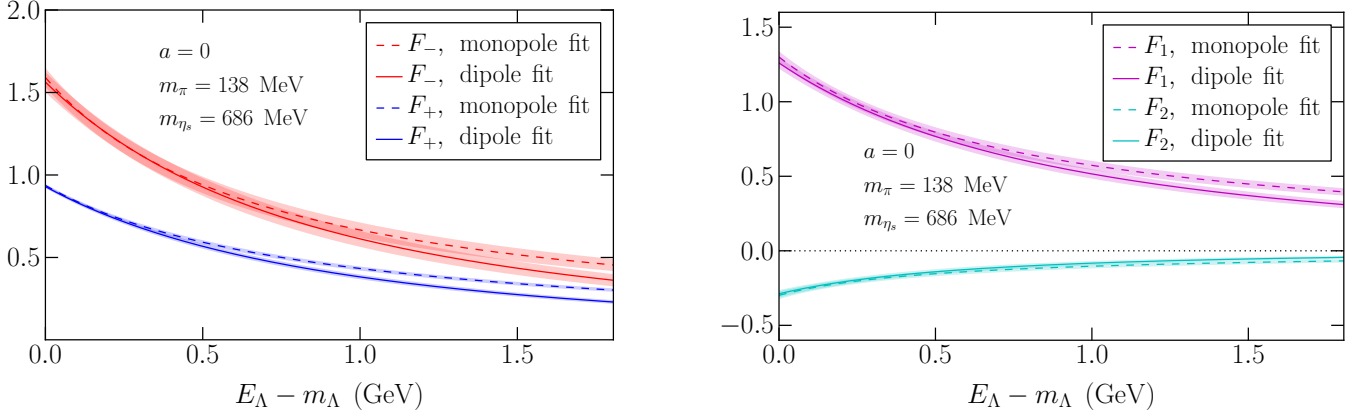


FIG. 14. Comparison of our results for the $\Lambda_Q \rightarrow \Lambda$ form factors from dipole fits using Eqs. (41) and (44) to results from monopole fits (the same equations without the power of 2 in the denominator). Shown here is the entire kinematic range needed for the decay $\Lambda_b \rightarrow \Lambda \ell^+ \ell^-$ with $m_\ell = 0$ (the point $q^2 = 0$ corresponds to $E_\Lambda - m_\Lambda \approx 1.8$ GeV). In the range where we have lattice data ($E_\Lambda - m_\Lambda \lesssim 0.7$ GeV), the dipole and monopole functions are consistent with each other, but for large $E_\Lambda - m_\Lambda$, model-dependence can be seen. In our main analysis we choose the dipole fits as they have slightly lower values of χ^2/dof .

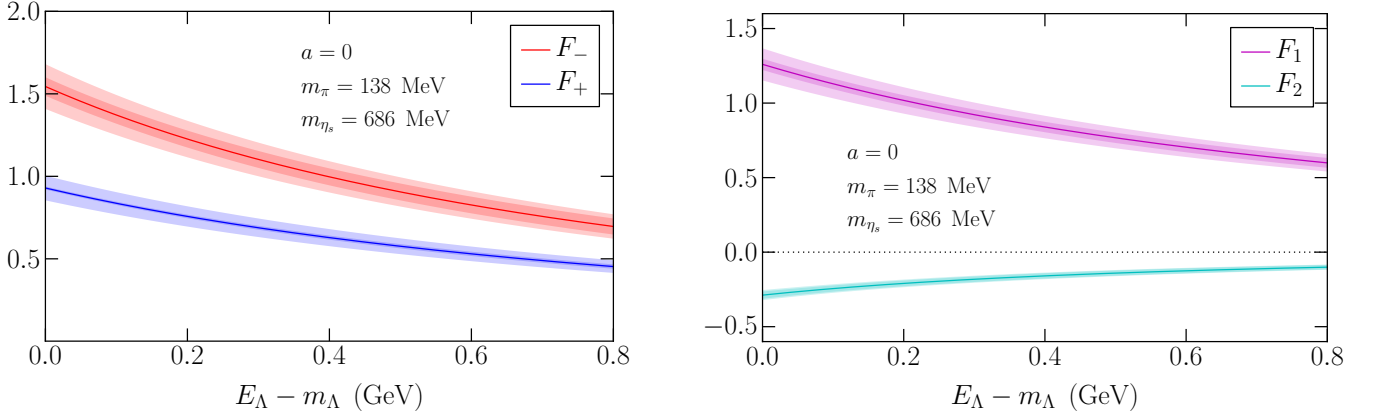


FIG. 15. Final results for the $\Lambda_Q \rightarrow \Lambda$ form factors, given by $F_\pm = N_\pm / (X_\pm + E_\Lambda - m_\Lambda)^2$ and $F_{1,2} = N_{1,2} / (X_{1,2} + E_\Lambda - m_\Lambda)^2$ with parameters as in Tables VIII and IX. The dark shaded bands show the statistical uncertainty, and the light shaded bands show the total (including 8% systematic) uncertainty. The results are renormalized in the $\overline{\text{MS}}$ scheme at $\mu = m_b$.

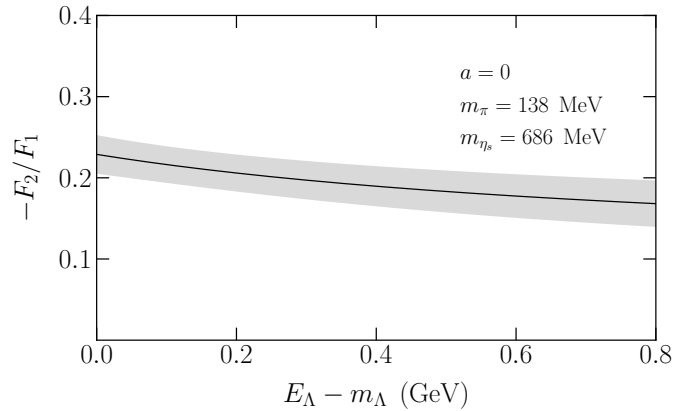


FIG. 16. Final results for the form factor ratio $-F_2/F_1$, given by $-(N_2/N_1)(X_1 + E_\Lambda - m_\Lambda)^2 / (X_2 + E_\Lambda - m_\Lambda)^2$ with parameters as in Table IX. The shaded band shows total uncertainty, which is dominated by the statistical uncertainty.

By “residual discretization errors” we mean discretization errors that are not eliminated through the continuum extrapolation using the factors of $[1 + d_{\pm}(a^i E_{\Lambda}^{i,n})^2]$ in Eq. (41) and $[1 + d_{1,2}(a^i E_{\Lambda}^{i,n})^2]$ in Eq. (44). While we know that the leading discretization orders are quadratic in a , we do not know how they depend on E_{Λ} . To study the effect of the factors $[1 + d_{\pm}(a^i E_{\Lambda}^{i,n})^2]$ and $[1 + d_{1,2}(a^i E_{\Lambda}^{i,n})^2]$, we perform new fits with d_{\pm} (or $d_{1,2}$) set to zero. In this case, the resulting changes in all form factors are less than 4% for $E_{\Lambda} - m_{\Lambda} < 0.8$ GeV, and are consistent with zero within the statistical uncertainties.

Combining the uncertainties in the above discussion, we estimate the total systematic uncertainty of our final results for the form factors for $E_{\Lambda} - m_{\Lambda} < 0.8$ GeV to be 8%. Plots of the form factors including this systematic uncertainty are shown in Fig. 15. The relatively large systematic uncertainty from the current matching cancels in ratios such as F_2/F_1 . This ratio is shown in Fig. 16, and we estimate the total systematic uncertainty in F_2/F_1 to be 5%.

IV. THE DECAY $\Lambda_b \rightarrow \Lambda \ell^+ \ell^-$

As a first application of our results for the $\Lambda_Q \rightarrow \Lambda$ form factors, we calculate the differential branching fraction for the decays $\Lambda_b \rightarrow \Lambda \ell^+ \ell^-$ with $\ell = e, \mu, \tau$ in the standard model. Long-distance contributions (discussed at the end of this section) are not included. In the following, it is convenient to use the notation

$$\mathcal{H}_{\text{eff}} = -\frac{2G_F}{\sqrt{2}} V_{tb} V_{ts}^* \sum_{i=7,9,10} \left(C_{i,\text{eff}}^V O_i^V - C_{i,\text{eff}}^A O_i^A \right), \quad (45)$$

with

$$\begin{aligned} O_7^V &= \frac{e}{16\pi^2} m_b \bar{s} \sigma^{\mu\nu} b F_{\mu\nu}^{(\text{e.m.})}, & O_7^A &= -\frac{e}{16\pi^2} m_b \bar{s} \sigma^{\mu\nu} \gamma_5 b F_{\mu\nu}^{(\text{e.m.})}, \\ O_9^V &= \frac{e^2}{16\pi^2} \bar{s} \gamma^{\mu} b \bar{l} \gamma_{\mu} l, & O_9^A &= \frac{e^2}{16\pi^2} \bar{s} \gamma^{\mu} \gamma_5 b \bar{l} \gamma_{\mu} l, \\ O_{10}^V &= \frac{e^2}{16\pi^2} \bar{s} \gamma^{\mu} b \bar{l} \gamma_{\mu} \gamma_5 l, & O_{10}^A &= \frac{e^2}{16\pi^2} \bar{s} \gamma^{\mu} \gamma_5 b \bar{l} \gamma_{\mu} \gamma_5 l, \end{aligned} \quad (46)$$

and

$$\begin{aligned} C_{i,\text{eff}}^V &= C_{i,\text{eff}} + C'_{i,\text{eff}}, \\ C_{i,\text{eff}}^A &= C_{i,\text{eff}} - C'_{i,\text{eff}}. \end{aligned} \quad (47)$$

The “effective” Wilson coefficients $C_{i,\text{eff}}$ and $C'_{i,\text{eff}}$ ($i = 7, 9, 10$), which are defined at the scale $\mu = m_b$, contain the one-loop matrix elements of the four-quark operators O_1, \dots, O_6 [4].

The invariant matrix element of \mathcal{H}_{eff} is given by

$$\begin{aligned} \mathcal{M} &= -\langle \Lambda(p', s') | \ell^+(p_+, s_+) \ell^-(p_-, s_-) | \mathcal{H}_{\text{eff}} | \Lambda_b(p, s) \rangle \\ &= \frac{G_F \alpha_{\text{em}}}{2\sqrt{2}\pi} V_{tb} V_{ts}^* \left[A_{\mu} \bar{u}(p_+, s_+) \gamma^{\mu} v(p_-, s_-) + B_{\mu} \bar{u}(p_+, s_+) \gamma^{\mu} \gamma_5 v(p_-, s_-) \right], \end{aligned}$$

with the hadronic matrix elements

$$\begin{aligned} A_{\mu} &= \langle \Lambda(p', s') | \left(C_{9,\text{eff}}^V(q^2) \bar{s} \gamma_{\mu} b - C_{9,\text{eff}}^A(q^2) \bar{s} \gamma_{\mu} \gamma_5 b - C_{7,\text{eff}}^V \frac{2m_b}{q^2} q^{\nu} \bar{s} i \sigma_{\mu\nu} b - C_{7,\text{eff}}^A \frac{2m_b}{q^2} q^{\nu} \bar{s} i \sigma_{\mu\nu} \gamma_5 b \right) | \Lambda_b(p, s) \rangle, \\ B_{\mu} &= \langle \Lambda(p', s') | \left(C_{10,\text{eff}}^V \bar{s} \gamma_{\mu} b - C_{10,\text{eff}}^A \bar{s} \gamma_{\mu} \gamma_5 b \right) | \Lambda_b(p, s) \rangle. \end{aligned} \quad (48)$$

Here we have contracted the electromagnetic field strength tensor in O_7^V and O_7^A with a perturbative insertion of the leptonic QED interaction term.

In order to use the HQET relation (3) to express the hadronic matrix elements in terms of the form factors F_1 and F_2 , we first need to match the QCD $b \rightarrow s$ currents in Eq. (48) to HQET currents. We use the one-loop perturbative results in naive dimensional regularization from Ref. [63]:

$$\begin{aligned} \bar{s} \gamma_{\mu} b &= c_{\gamma} \bar{s} \gamma_{\mu} Q + c_v \bar{s} v_{\mu} Q, \\ \bar{s} \gamma_{\mu} \gamma_5 b &= c_{\gamma} \bar{s} \gamma_{\mu} \gamma_5 Q - c_v \bar{s} v_{\mu} \gamma_5 Q, \\ \bar{s} \sigma_{\mu\nu} b &= c_{\sigma} \bar{s} \sigma_{\mu\nu} Q, \\ \bar{s} \sigma_{\mu\nu} \gamma_5 b &= c_{\sigma} \bar{s} \sigma_{\mu\nu} \gamma_5 Q, \end{aligned} \quad (49)$$

with

$$\begin{aligned} c_\gamma &= 1 - \frac{\alpha_s(\mu)}{\pi} \left[\frac{4}{3} + \ln \left(\frac{\mu}{m_b} \right) \right], \\ c_v &= \frac{2}{3} \frac{\alpha_s(\mu)}{\pi}, \\ c_\sigma &= 1 - \frac{\alpha_s(\mu)}{\pi} \left[\frac{4}{3} + \frac{5}{3} \ln \left(\frac{\mu}{m_b} \right) \right]. \end{aligned} \quad (50)$$

This gives

$$\begin{aligned} A_\mu &= \bar{u}(p', s') \left(F_1 + \not{p} F_2 \right) \left(C_{9,\text{eff}}^V(q^2) c_\gamma \gamma_\mu + C_{9,\text{eff}}^V(q^2) c_v v_\mu - C_{9,\text{eff}}^A(q^2) c_\gamma \gamma_\mu \gamma_5 + C_{9,\text{eff}}^A(q^2) c_v v_\mu \gamma_5 \right. \\ &\quad \left. - C_{7,\text{eff}}^V c_\sigma \frac{2m_b}{q^2} q^\nu i \sigma_{\mu\nu} - C_{7,\text{eff}}^A c_\sigma \frac{2m_b}{q^2} q^\nu i \sigma_{\mu\nu} \gamma_5 \right) u(p, s), \\ B_\mu &= \bar{u}(p', s') \left(F_1 + \not{p} F_2 \right) \left(C_{10,\text{eff}}^V c_\gamma \gamma_\mu + C_{10,\text{eff}}^V c_v v_\mu - C_{10,\text{eff}}^A c_\gamma \gamma_\mu \gamma_5 + C_{10,\text{eff}}^A c_v v_\mu \gamma_5 \right) u(p, s). \end{aligned} \quad (51)$$

Note that here we use spinors with the standard relativistic normalization for all particles, including the Λ_b . In terms of the HQET spinors (7), we have $u(p, s) = \sqrt{m_{\Lambda_b}} \mathcal{U}(v, s)$, with $p = m_{\Lambda_b} v$. For a given value of q^2 , the form factors F_1 and F_2 in Eq. (51) are evaluated at

$$E_\Lambda = p' \cdot v = \frac{m_{\Lambda_b}^2 + m_\Lambda^2 - q^2}{2m_{\Lambda_b}}, \quad (52)$$

where the masses take their physical values. The fully differential decay rate with polarized particles is given by

$$d\Gamma = \frac{1}{2m_{\Lambda_b}} \frac{d^3 p'}{(2\pi)^3 2E_\Lambda} \frac{d^3 p_-}{(2\pi)^3 2E_{\ell^-}} \frac{d^3 p_+}{(2\pi)^3 2E_{\ell^+}} (2\pi)^4 \delta^4(p - p' - p_- - p_+) |\mathcal{M}|^2. \quad (53)$$

For the standard model calculation, we set the right-handed couplings to zero ($C_{7,\text{eff}}' = C_{9,\text{eff}}' = C_{10,\text{eff}}' = 0$) and use the following Wilson coefficients (at $\mu = 4.8$ GeV), which are of next-to-next-to-leading-logarithm accuracy [64]:

$$\begin{aligned} C_{7,\text{eff}} &= -0.304, \\ C_{9,\text{eff}}(q^2) &= 4.211 + Y(q^2), \\ C_{10,\text{eff}} &= -4.103. \end{aligned} \quad (54)$$

The function $Y(q^2)$ is defined as in Ref. [64]. Furthermore, we use $|V_{ts}| = 0.04002$ and $|V_{tb}| = 0.999142$ from Ref. [65].

To calculate $d\Gamma/dq^2$, we integrate (53) over the lepton momenta and the direction of the Λ , sum over the spins of the Λ , ℓ^+ , ℓ^- , and average over the Λ_b spin (because $d\Gamma/dq^2$ is rotationally symmetric, it has to be independent of the Λ_b polarization, and therefore we can treat the Λ_b as unpolarized here). The result is given by

$$\begin{aligned} \frac{d\Gamma}{dq^2} &= \frac{\alpha_{\text{em}}^2 G_F^2 |V_{tb} V_{ts}^*|^2}{6144 \pi^5 q^4 m_{\Lambda_b}^5} \sqrt{1 - \frac{4m_l^2}{q^2}} \sqrt{((m_{\Lambda_b} - m_\Lambda)^2 - q^2)((m_{\Lambda_b} + m_\Lambda)^2 - q^2)} \\ &\quad \times \left[q^2 |C_{10,\text{eff}}|^2 \mathcal{A}_{10,10} + 16c_\sigma^2 m_b^2 (q^2 + 2m_l^2) |C_{7,\text{eff}}|^2 \mathcal{A}_{7,7} + q^2 (q^2 + 2m_l^2) |C_{9,\text{eff}}(q^2)|^2 \mathcal{A}_{9,9} \right. \\ &\quad \left. + 8q^2 c_\sigma m_b (q^2 + 2m_l^2) m_{\Lambda_b} \Re[C_{7,\text{eff}} C_{9,\text{eff}}(q^2)] \mathcal{A}_{7,9} \right], \end{aligned} \quad (55)$$

with

$$\begin{aligned} \mathcal{A}_{10,10} &= \left[(2c_\gamma^2 + 2c_\gamma c_v + c_v^2) (2m_l^2 + q^2) \left(m_{\Lambda_b}^4 - 2m_{\Lambda_b}^2 m_\Lambda^2 + (q^2 - m_\Lambda^2)^2 \right) \right. \\ &\quad \left. + 2m_{\Lambda_b}^2 q^2 (4c_\gamma^2 (q^2 - 4m_l^2) - (2c_\gamma c_v + c_v^2) (q^2 - 10m_l^2)) \right] \mathcal{F} + 4c_\gamma (c_\gamma + c_v) (2m_l^2 + q^2) \mathcal{G} F_+ F_-, \end{aligned} \quad (56)$$

$$\mathcal{A}_{7,7} = \left(m_{\Lambda_b}^4 + m_{\Lambda_b}^2 (q^2 - 2m_\Lambda^2) + (q^2 - m_\Lambda^2)^2 \right) \mathcal{F} + 2\mathcal{G} F_+ F_-, \quad (57)$$

$$\begin{aligned} \mathcal{A}_{9,9} &= \left[(2c_\gamma^2 + 2c_\gamma c_v + c_v^2) \left(m_{\Lambda_b}^4 + (q^2 - m_\Lambda^2)^2 \right) - 2m_{\Lambda_b}^2 (2c_\gamma^2 (m_\Lambda^2 - 2q^2) + (2c_\gamma c_v + c_v^2) (m_\Lambda^2 + q^2)) \right] \mathcal{F} \\ &\quad + 4c_\gamma (c_\gamma + c_v) \mathcal{G} F_+ F_-, \end{aligned} \quad (58)$$

$$\mathcal{A}_{7,9} = 3c_\gamma (m_{\Lambda_b}^2 - m_\Lambda^2 + q^2) \mathcal{F} + 2(3c_\gamma + c_v) \left(m_\Lambda^4 - 2m_\Lambda^2 (m_{\Lambda_b}^2 + q^2) + (q^2 - m_{\Lambda_b}^2)^2 \right) F_+ F_-, \quad (59)$$

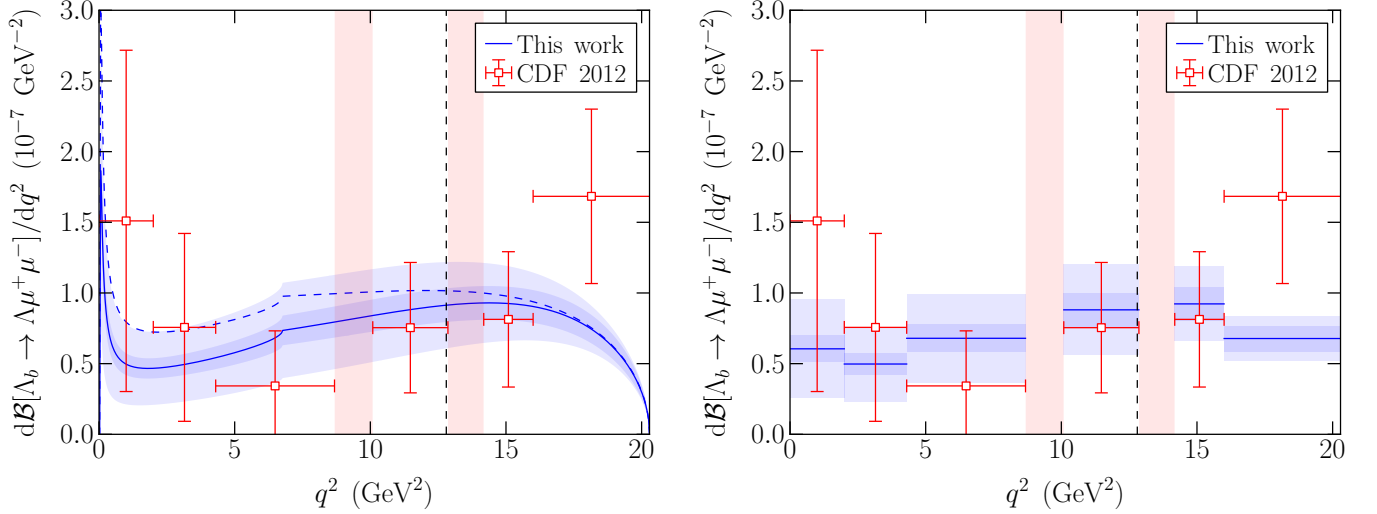


FIG. 17. Left panel: Differential branching fraction for $\Lambda_b \rightarrow \Lambda \mu^+ \mu^-$. The solid curve is our prediction using the form factors from lattice QCD. Long-distance effects are not included in the calculation. The inner, dark shaded band around the curve indicates the uncertainty in $d\mathcal{B}/dq^2$ that results from the statistical plus systematic uncertainty in the form factors F_{\pm} . The outer, light shaded band additionally includes an estimate of the systematic uncertainty in $d\mathcal{B}/dq^2$ that results from our use of the static approximation for the b quark. The vertical dashed line indicates the lowest value of q^2 where we have lattice data; to the left of that line the form factors are extrapolated. To illustrate the model-dependence resulting from the extrapolation of the form factors to low q^2 , the dashed curve shows $d\mathcal{B}/dq^2$ computed with form factors extrapolated using a different ansatz (monopole instead of dipole, see Fig. 14; the uncertainty for the dashed curve is not shown for clarity). The experimental data are from Ref. [67], which is an update of Ref. [10]. The error bars shown for the experimental data include systematic uncertainties. The vertical shaded bands indicate the charmonium veto regions, where long-distance effects are large. Right panel: with binning applied to the theory prediction.

where

$$\mathcal{F} = ((m_{\Lambda_b} - m_{\Lambda})^2 - q^2)F_-^2 + ((m_{\Lambda_b} + m_{\Lambda})^2 - q^2)F_+^2, \quad (60)$$

$$\mathcal{G} = m_{\Lambda_b}^6 - m_{\Lambda_b}^4 (3m_{\Lambda}^2 + q^2) - m_{\Lambda_b}^2 (q^2 - m_{\Lambda}^2) (3m_{\Lambda}^2 + q^2) + (q^2 - m_{\Lambda}^2)^3. \quad (61)$$

To obtain the differential branching fraction $d\mathcal{B}/dq^2 = \tau_{\Lambda_b} d\Gamma/dq^2$, we use the experimental value of the Λ_b lifetime, $\tau_{\Lambda_b} = 1.425 \cdot 10^{-12}$ s [66]. The form factors F_+ and F_- are given by the functions (43) with parameters N_{\pm} and X_{\pm} as in Table VIII, and with additional systematic uncertainties of 8% included (see Fig. 15). The resulting differential branching fraction for $\Lambda_b \rightarrow \Lambda \mu^+ \mu^-$ is shown in Fig. 17, along with recent experimental results from CDF [67]. The agreement of the standard model with the experimental data is clear, with no evidence for physics beyond the standard model. Further predictions for $\Lambda_b \rightarrow \Lambda \ell^+ \ell^-$ with $\ell = e, \tau$ are shown in Fig. 18.

In Figs. 17 and 18, the inner shaded bands around the curves correspond to the statistical plus systematic uncertainty in the form factors F_{\pm} . However, note that we have lattice data only in the region $q^2 \gtrsim 13$ GeV², as indicated by the vertical dashed lines in Figs. 17 and 18. Below that region, we rely on extrapolations of the form factors, which are model-dependent. This was shown in Fig. 14, where we compared the form factors from dipole and monopole fits. Our main results for the differential branching fractions are based on the dipole form factors. To illustrate the model-dependence, the dashed curves in Figs. 17 and 18 give the differential branching fractions calculated with the monopole form factors (the uncertainties of the dashed curves are not shown for clarity, but are of similar size as with the dipole form factors). In the large- q^2 region, both curves are consistent with each other. At low q^2 , model-dependence can be seen, but as already discussed in Sec. III G, a comparison between any two fit models can only give a qualitative picture of the model-dependence.

The outer shaded bands in Figs. 17 and 18 include an estimate of the systematic uncertainty in $d\mathcal{B}/dq^2$ which arises from the use of the static approximation (i.e., leading-order HQET) for the b quark. In general, the uncertainty associated with this approximation is of order Λ_{QCD}/m_b . However, the non-zero momentum \mathbf{p}' of the Λ baryon in the Λ_b rest frame is an additional relevant scale, which may lead to errors of order $|\mathbf{p}'|/m_b$. Thus, we add these two

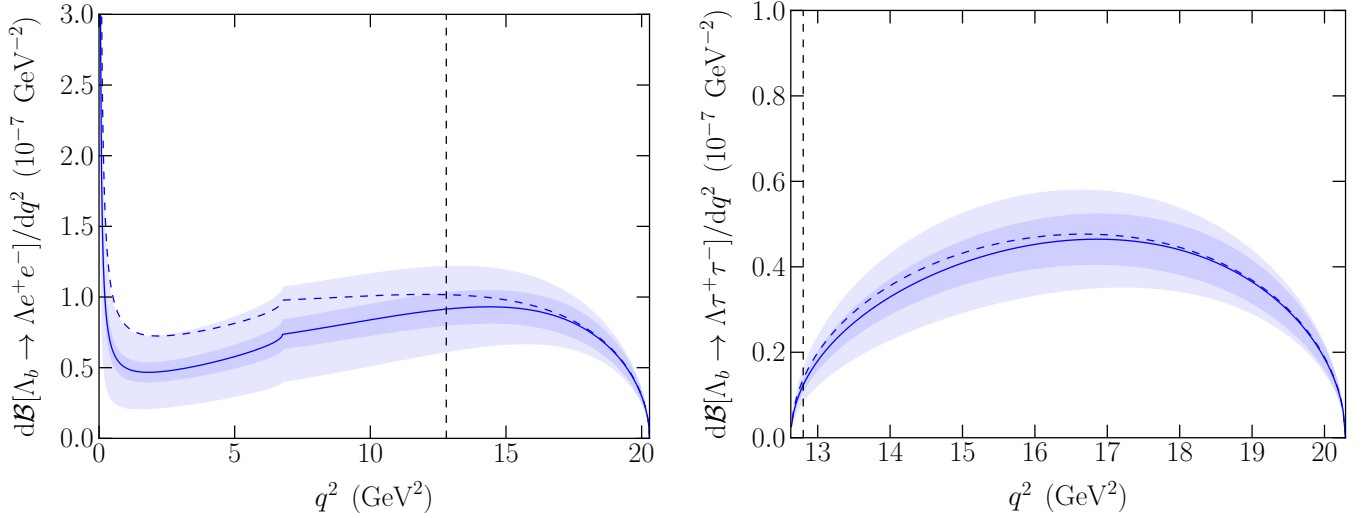


FIG. 18. Differential branching fractions for $\Lambda_b \rightarrow \Lambda e^+ e^-$ (left) and $\Lambda_b \rightarrow \Lambda \tau^+ \tau^-$ (right). See the caption of Fig. 17 for explanations.

errors in quadrature and estimate the relative systematic uncertainty in $d\mathcal{B}/dq^2$ due to the use of HQET to be

$$\sqrt{\frac{\Lambda_{\text{QCD}}^2}{m_b^2} + \frac{|\mathbf{p}'|^2}{m_b^2}}, \quad (62)$$

where we take $\Lambda_{\text{QCD}} = 500$ MeV.

Another major cause of systematic uncertainty in the branching fraction is that we have neglected long-distance effects. The most important type of long-distance effects is associated with photon exchange between the lepton and quark electromagnetic currents, where the quark electromagnetic current combines with the four-quark operators O_1 to O_6 in the effective Hamiltonian (1). The resulting contribution to the decay amplitude is described by nonlocal hadronic matrix elements of the form

$$\frac{1}{q^2} \int d^4x e^{iq \cdot x} \langle \Lambda(p', s') | T O_i(0) j_{\text{e.m.}}^\mu(x) | \Lambda_b(p, s) \rangle, \quad (63)$$

where $j_{\text{e.m.}}^\mu(x)$ is the quark electromagnetic current (see for example [68, 69]). These are challenging matrix elements to compute from lattice QCD, but may give large contributions when $\sqrt{q^2}$ coincides with the mass of a hadronic resonance with $J^{PC} = 1^{--}$. Of the four-quark operators, $O_1 = (\bar{c}^b \gamma^\mu P_L b^a)(\bar{s}^a \gamma_\mu P_L c^b)$ and $O_2 = (\bar{c}^a \gamma^\mu P_L b^a)(\bar{s}^b \gamma_\mu P_L c^b)$ (where the superscripts a and b are color indices) have the largest Wilson coefficients, and at $q^2 = m_{J/\psi}^2, m_{\psi'}^2$, the decay amplitude is dominated by the non-local matrix elements of O_1 and O_2 . The experimental analysis of Ref. [67] excludes these q^2 regions, as shown by the vertical shaded bands in Fig. 17. Away from these resonances, however, we expect the short distance contributions from $O_{7,9,10}$ to be the most important. Several approaches show that for large q^2 , these and other long-distance effects can be treated as small corrections to the leading order behavior given by matrix elements of $O_{7,9,10}$ [68–70]. Although these papers discuss $B \rightarrow K^{(*)} \ell^+ \ell^-$, the same principles apply to $\Lambda_b \rightarrow \Lambda \ell^+ \ell^-$.

V. CONCLUSIONS

Theoretical studies of the rare baryon decays $\Lambda_b \rightarrow \Lambda \ell^+ \ell^-$ and $\Lambda_b \rightarrow \Lambda \gamma$ require knowledge of the hadronic matrix elements $\langle \Lambda | \bar{s} \Gamma b | \Lambda_b \rangle$ in nonperturbative QCD. At leading order in heavy-quark effective theory, these matrix elements are given by two independent form factors, F_1 and F_2 (or, equivalently, $F_+ = F_1 + F_2$ and $F_- = F_1 - F_2$), which are functions of the energy of the Λ baryon in the Λ_b rest frame [33–35]. Here, we have performed the first lattice QCD calculation of these form factors. Our final results for F_\pm and $F_{1,2}$, in the continuum limit and for the physical values of the up, down, and strange-quark masses, are shown in Fig. 15. High precision determinations were achieved by analyzing the ratios $R_+(\mathbf{p}'^2, t)$ and $R_-(\mathbf{p}'^2, t)$, defined in Eqs. (32) and (33), for a wide range of

source-sink separations t , and by using multiple light-quark masses as well as two different lattice spacings. Systematic uncertainties in the form factors are estimated to be $\sim 8\%$. A further reduction in systematic uncertainties would require two-loop or nonperturbative current matching, finer lattice spacings, and light-quark masses at or very close to the physical values (which would also require increased lattice sizes). However, already at our current level of uncertainty in the form factors, the precision in phenomenological applications is primarily limited by the use of leading-order HQET for the heavy quark.

To compare our form factor results to the literature, let us first consider the zero recoil point ($E_\Lambda = m_\Lambda$, or $q^2 = q_{\text{max}}^2$). There we obtain (matched to the $\overline{\text{MS}}$ scheme at $\mu = m_b$)

$$\begin{aligned} F_1(q_{\text{max}}^2) &= 1.26(4)(10), \\ F_2(q_{\text{max}}^2) &= -0.288(25)(23), \\ F_2(q_{\text{max}}^2)/F_1(q_{\text{max}}^2) &= -0.229(21)(11), \end{aligned} \tag{64}$$

where the first uncertainty is statistical/fitting, and the second uncertainty is systematic. The ratio F_2/F_1 has previously been estimated by the CLEO collaboration using experimental data for the semileptonic $\Lambda_c \rightarrow \Lambda e^+ \nu_e$ decay, assuming the same shape for F_1 and F_2 and ignoring Λ_{QCD}/m_c corrections, to be $F_2/F_1 = -0.31(5)(4)$ [45]. This is consistent with our results, given the expected size of Λ_{QCD}/m_c corrections, but significantly less precise. In Ref. [38], an earlier CLEO extraction of F_2/F_1 [44] was combined with the MIT bag model to obtain $F_1(q_{\text{max}}^2) = 1.02$, $F_2(q_{\text{max}}^2) = -0.34$. The authors of Ref. [23] combined the CLEO data from Ref. [44] with the measured Λ_c lifetime to get $F_1(q_{\text{max}}^2) = 1.21$, $F_2(q_{\text{max}}^2) = -0.30$, which happen to be quite close to our results. The sum rule calculation of Ref. [25] gave $F_1(q_{\text{max}}^2) \approx 0.81$, $F_2(q_{\text{max}}^2) \approx -0.34$, and $F_2(q_{\text{max}}^2)/F_1(q_{\text{max}}^2) \approx -0.42$, in marked disagreement with (64).

At large recoil, leading-order soft-collinear effective theory predicts that F_1 becomes equal to a soft form factor ξ_Λ , while F_2 vanishes [27, 36, 37]. Using light-cone sum rules, the authors of Ref. [36] obtained $\xi_\Lambda(q^2 = 0) \approx 0.38$. This is rather close to our results for F_1 at that point ($q^2 = 0$ corresponds to $E_\Lambda - m_\Lambda \approx 1.8$ GeV), as can be seen in Fig. (14). However, we stress that our results are not reliable at such large values of $E_\Lambda - m_\Lambda$, where we do not have lattice data and rely on extrapolation.

Our form factor results can be used to make theoretical predictions for several observables in $\Lambda_b \rightarrow \Lambda \ell^+ \ell^-$ decays. As a first example, here we have calculated the differential branching fractions of these decays in the standard model. For $\ell = \mu$, experimental data are already available from CDF [67], and our calculation agrees with the data within uncertainties (see Fig. 17). The theoretical uncertainties in the branching fraction are dominated by errors of order Λ_{QCD}/m_b and $|\mathbf{p}'|/m_b$ associated with the use of leading-order HQET for the heavy quark, and by missing long-distance contributions to the decay amplitudes. At high recoil, there is also an unknown uncertainty associated with the extrapolation of the form factors. The long-distance contributions have not been calculated in lattice QCD, and need to be estimated using other approaches. The HQET uncertainties could be reduced by using higher-order lattice HQET, lattice nonrelativistic QCD, or a relativistic action for the b quarks. In such calculations one would have to deal with more complicated current matching and the full set of ten $\Lambda_b \rightarrow \Lambda$ form factors.

Another possible application of our form factor results to the phenomenology of $\Lambda_b \rightarrow \Lambda \ell^+ \ell^-$ decays is to study various angular distributions which depend on the baryon polarization and probe the helicity structure of the effective weak Hamiltonian. In particular, one should compute the angular distribution of the two-stage decay $\Lambda_b \rightarrow (\Lambda \rightarrow p\pi^-) \ell^+ \ell^-$ for partially polarized Λ_b baryons. To make numerical predictions of these angular distributions for the LHC, the polarization of the Λ_b baryons produced in proton-proton collisions needs to be determined, for example using the method discussed in Ref. [20]. It remains to be seen whether the decay $\Lambda_b \rightarrow (\Lambda \rightarrow p\pi^-) \ell^+ \ell^-$ will be competitive with $B \rightarrow K^*(\rightarrow K\pi) \ell^+ \ell^-$ [64] in constraining new-physics models.

ACKNOWLEDGMENTS

We thank the RBC and UKQCD collaborations for access to their gauge field configurations. The domain-wall propagators used in this work were computed with the Chroma software system [71]. This work is supported by the U.S. Department of Energy under cooperative research agreement Contract Number DE-FG02-94ER40818. Numerical calculations were performed using resources at the National Energy Research Scientific Computing Center (U.S. Department of Energy Grant Number DE-AC02-05CH11231), and XSEDE resources at the National Institute for Computational Sciences (National Science Foundation Grant Number OCI-1053575). The work of WD was supported in part by the Jeffress Memorial Trust, J-968. WD and SM were also supported by DOE Outstanding Junior Investigator Award DE-SC000-1784. CJDL is supported by Taiwanese NSC Grant Number 99-2112-M-009-004-MY3. MW is supported by the STFC and received additional travel support from an IPPP Associateship.

-
- [1] B. Grinstein, M. J. Savage, and M. B. Wise, Nucl. Phys. B **319**, 271 (1989).
 - [2] B. Grinstein, R. P. Springer, and M. B. Wise, Nucl. Phys. B **339**, 269 (1990).
 - [3] M. Misiak, Nucl. Phys. B **393**, 23 (1993) [Erratum-ibid. B **439**, 461 (1995)].
 - [4] A. J. Buras, M. Misiak, M. Münz, and S. Pokorski, Nucl. Phys. B **424**, 374 (1994) [arXiv:hep-ph/9311345].
 - [5] A. J. Buras and M. Münz, Phys. Rev. D **52**, 186 (1995) [arXiv:hep-ph/9501281].
 - [6] G. Buchalla, A. J. Buras, and M. E. Lautenbacher, Rev. Mod. Phys. **68**, 1125 (1996) [arXiv:hep-ph/9512380].
 - [7] K. G. Chetyrkin, M. Misiak, and M. Münz, Phys. Lett. B **400**, 206 (1997) [Erratum-ibid. B **425**, 414 (1998)] [arXiv:hep-ph/9612313].
 - [8] C. Bobeth, M. Misiak, and J. Urban, Nucl. Phys. B **574**, 291 (2000) [arXiv:hep-ph/9910220].
 - [9] W. Altmannshofer and D. M. Straub, JHEP **1208**, 121 (2012) [arXiv:1206.0273].
 - [10] T. Aaltonen *et al.* (CDF Collaboration), Phys. Rev. Lett. **107**, 201802 (2011) [arXiv:1107.3753].
 - [11] A. F. Falk and M. E. Peskin, Phys. Rev. D **49**, 3320 (1994) [arXiv:hep-ph/9308241].
 - [12] G. Bonvicini and L. Randall, Phys. Rev. Lett. **73**, 392 (1994) [arXiv:hep-ph/9401299].
 - [13] C. Diaconu, M. Talby, J. G. Körner, and D. Pirjol, Phys. Rev. D **53**, 6186 (1996) [arXiv:hep-ph/9512330].
 - [14] D. Buskulic *et al.* (ALEPH Collaboration), Phys. Lett. B **365**, 437 (1996).
 - [15] G. Abbiendi *et al.* (OPAL Collaboration), Phys. Lett. B **444**, 539 (1998) [arXiv:hep-ex/9808006].
 - [16] P. Abreu *et al.* (DELPHI Collaboration), Phys. Lett. B **474**, 205 (2000).
 - [17] Z. J. Ajaltouni, E. Conte, and O. Leitner, Phys. Lett. B **614**, 165 (2005) [arXiv:hep-ph/0412116].
 - [18] W. G. D. Dharmaratna and G. R. Goldstein, Phys. Rev. D **53**, 1073 (1996).
 - [19] G. Hiller, M. Knecht, F. Legger, and T. Schietinger, Phys. Lett. B **649**, 152 (2007) [arXiv:hep-ph/0702191].
 - [20] J. Hrivnac, R. Lednicky, and M. Smizanska, J. Phys. G **21**, 629 (1995) [arXiv:hep-ph/9405231].
 - [21] M. Gremm, F. Krüger, and L. M. Sehgal, Phys. Lett. B **355**, 579 (1995) [arXiv:hep-ph/9505354].
 - [22] G. Hiller and A. Kagan, Phys. Rev. D **65**, 074038 (2002) [arXiv:hep-ph/0108074].
 - [23] T. Mannel and S. Recksiegel, J. Phys. G **24**, 979 (1998) [arXiv:hep-ph/9701399].
 - [24] C.-K. Chua, X.-G. He, and W.-S. Hou, Phys. Rev. D **60**, 014003 (1999) [arXiv:hep-ph/9808431].
 - [25] C.-S. Huang and H.-G. Yan, Phys. Rev. D **59**, 114022 (1999) [Erratum-ibid. D **61**, 039901 (2000)] [arXiv:hep-ph/9811303].
 - [26] Y.-M. Wang, Y. Li, and C.-D. Lu, Eur. Phys. J. C **59**, 861 (2009) [arXiv:0804.0648].
 - [27] T. Mannel and Y.-M. Wang, JHEP **1112**, 067 (2011) [arXiv:1111.1849].
 - [28] C.-H. Chen and C. Q. Geng, Phys. Rev. D **63**, 114024 (2001) [arXiv:hep-ph/0101171].
 - [29] C.-H. Chen, C. Q. Geng, and J. N. Ng, Phys. Rev. D **65**, 091502 (2002) [arXiv:hep-ph/0202103].
 - [30] M. J. Aslam, Y.-M. Wang, and C.-D. Lu, Phys. Rev. D **78**, 114032 (2008) [arXiv:0808.2113].
 - [31] C.-H. Chen and C. Q. Geng, Phys. Lett. B **516**, 327 (2001) [arXiv:hep-ph/0101201].
 - [32] C.-H. Chen and C. Q. Geng, Phys. Rev. D **64**, 074001 (2001) [arXiv:hep-ph/0106193].
 - [33] T. Mannel, W. Roberts, and Z. Ryzak, Nucl. Phys. B **355**, 38 (1991).
 - [34] F. Hussain, J. G. Körner, M. Kramer, and G. Thompson, Z. Phys. C **51**, 321 (1991).
 - [35] F. Hussain, D.-S. Liu, M. Kramer, J. G. Körner, and S. Tawfiq, Nucl. Phys. B **370**, 259 (1992).
 - [36] T. Feldmann and M. W. Y. Yip, Phys. Rev. D **85**, 014035 (2012) [Erratum-ibid. D **86**, 079901 (2012)] [arXiv:1111.1844].
 - [37] W. Wang, Phys. Lett. B **708**, 119 (2012) [arXiv:1112.0237].
 - [38] H.-Y. Cheng, C.-Y. Cheung, G.-L. Lin, Y. C. Lin, T.-M. Yan, and H.-L. Yu, Phys. Rev. D **51**, 1199 (1995) [arXiv:hep-ph/9407303].
 - [39] H.-Y. Cheng and B. Tseng, Phys. Rev. D **53**, 1457 (1996) [Erratum-ibid. D **55**, 1697 (1997)] [arXiv:hep-ph/9502391].
 - [40] R. Mohanta, A. K. Giri, M. P. Khanna, M. Ishida, and S. Ishida, Prog. Theor. Phys. **102**, 645 (1999) [arXiv:hep-ph/9908291].
 - [41] L. Mott and W. Roberts, Int. J. Mod. Phys. A **27**, 1250016 (2012) [arXiv:1108.6129].
 - [42] X.-G. He, T. Li, X.-Q. Li, and Y.-M. Wang, Phys. Rev. D **74**, 034026 (2006) [arXiv:hep-ph/0606025].
 - [43] Y.-M. Wang, Y.-L. Shen, and C.-D. Lu, Phys. Rev. D **80**, 074012 (2009) [arXiv:0907.4008].
 - [44] G. D. Crawford *et al.* (CLEO Collaboration), Phys. Rev. Lett. **75**, 624 (1995).
 - [45] J. W. Hinson *et al.* (CLEO Collaboration), Phys. Rev. Lett. **94**, 191801 (2005) [arXiv:hep-ex/0501002].
 - [46] W. Detmold, C. J. D. Lin, S. Meinel, and M. Wingate, PoS LATTICE **2012**, 123 (2012) [arXiv:1211.5127].
 - [47] E. Eichten and B. R. Hill, Phys. Lett. B **240**, 193 (1990).
 - [48] D. B. Kaplan, Phys. Lett. B **288**, 342 (1992) [arXiv:hep-lat/9206013].
 - [49] Y. Shamir, Nucl. Phys. B **406**, 90 (1993) [arXiv:hep-lat/9303005].
 - [50] V. Furman and Y. Shamir, Nucl. Phys. B **439**, 54 (1995) [arXiv:hep-lat/9405004].
 - [51] Y. Aoki *et al.* (RBC/UKQCD Collaboration), Phys. Rev. D **83**, 074508 (2011) [arXiv:1011.0892].
 - [52] A. Hasenfratz and F. Knechtli, Phys. Rev. D **64**, 034504 (2001) [arXiv:hep-lat/0103029].
 - [53] M. Della Morte, S. Dürr, J. Heitger, H. Molke, J. Rolf, A. Shindler, and R. Sommer (ALPHA Collaboration), Phys. Lett. B **581**, 93 (2004) [Erratum-ibid. B **612**, 313 (2005)] [arXiv:hep-lat/0307021].
 - [54] Y. Iwasaki, Report No. UTHEP-118 (1983).
 - [55] Y. Iwasaki and T. Yoshie, Phys. Lett. B **143**, 449 (1984).
 - [56] T. Ishikawa, Y. Aoki, J. M. Flynn, T. Izubuchi, and O. Laktik, JHEP **1105**, 040 (2011) [arXiv:1101.1072].
 - [57] X.-D. Ji and M. J. Musolf, Phys. Lett. B **257**, 409 (1991).

- [58] D. J. Broadhurst and A. G. Grozin, Phys. Lett. B **267**, 105 (1991) [arXiv:hep-ph/9908362].
- [59] K. C. Bowler *et al.* (UKQCD Collaboration), Phys. Rev. D **57**, 6948 (1998) [arXiv:hep-lat/9709028].
- [60] S. Meinel, Phys. Rev. D **82**, 114502 (2010) [arXiv:1007.3966].
- [61] C. T. H. Davies *et al.* (HPQCD Collaboration), Phys. Rev. D **81**, 034506 (2010) [arXiv:0910.1229].
- [62] M. Della Morte, A. Shindler, and R. Sommer, JHEP **0508**, 051 (2005) [arXiv:hep-lat/0506008].
- [63] E. Eichten and B. R. Hill, Phys. Lett. B **234**, 511 (1990).
- [64] W. Altmannshofer, P. Ball, A. Bharucha, A. J. Buras, D. M. Straub, and M. Wick, JHEP **0901**, 019 (2009) [arXiv:0811.1214].
- [65] J. Charles *et al.* (CKMfitter Group), “Updated results on the CKM matrix, including results presented up to ICHEP 2012” (http://ckmfitter.in2p3.fr/www/results/plots_ichep12/num/ckmEval_results_ICHEP12.pdf).
- [66] J. Beringer *et al.* (Particle Data Group Collaboration), Phys. Rev. D **86**, 010001 (2012).
- [67] CDF Collaboration, “Precise measurements of exclusive $b \rightarrow s\mu^+\mu^-$ decay amplitudes using the full CDF data set”, Public Note 108xx, Version 0.1 (<http://www-cdf.fnal.gov/physics/new/bottom/bottom.html>).
- [68] B. Grinstein and D. Pirjol, Phys. Rev. D **70**, 114005 (2004) [arXiv:hep-ph/0404250].
- [69] M. Beylich, G. Buchalla, and T. Feldmann, Eur. Phys. J. C **71**, 1635 (2011) [arXiv:1101.5118].
- [70] M. Beneke, T. Feldmann, and D. Seidel, Nucl. Phys. B **612**, 25 (2001) [arXiv:hep-ph/0106067].
- [71] R. G. Edwards and B. Joó, Nucl. Phys. Proc. Suppl. **140**, 832 (2005) [arXiv:hep-lat/0409003].